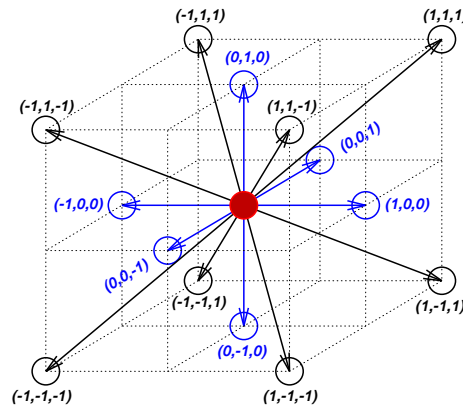


Dreidimensionale parallele
Lattice Boltzmann
Hydrodynamiksimulationen
turbulenter Strömungen in
interstellaren Dunkelwolken

Three-Dimensional Parallel
Lattice Boltzmann
Hydrodynamic Simulations
of Turbulent Flows in
Interstellar Dark Clouds



Inaugural-Dissertation
zur
Erlangung der Doktorwürde
der
Hohen Mathematisch-Naturwissenschaftlichen Fakultät
der
Rheinischen Friedrich-Wilhelms-Universität
zu
Bonn

vorgelegt
von
Dirk Muders
aus
Niederburg

Bonn
Juli 1995

Referent: Prof. Dr. J. Schmid-Burgk, MPIfR
Koreferent: Prof. Dr. H.-J. Fahr, Universität Bonn
Tag der Promotion: 25. August 1995

Meinen Eltern gewidmet

नितान्तनीलोत्पलपत्रकान्तिभिः
क्वचित्प्रभिन्नाञ्जनराशिसंनिभैः ।
क्वचित्सगर्भप्रमदास्तनप्रभैः
समाचितं व्योम घनैः समन्ततः ॥

इति श्रीकालिदासर्तुसंहारप्रावृङ्गवर्णने २ ।

Gleich eines dunklen Lotus blauem Schimmer
Hat rings mit Wolken sich die Luft umhüllt,
Die bald wie Frauen Zwillingsbrust erglänzen
Und bald wie eines Elefanten Bild.

ZWEITER VERS IN DER SCHILDERUNG DER REGENZEIT
AUS DEM JAHRESZEITENZYKLUS DES EHRWÜRDIGEN KĀLIDĀSA.

DEUTSCH VON PETER VON BOHLEN (1840).

A lustrous deep blue, like the lotus petal's hue,
With powdered eye-black in the distance seems to blend,
While over here glows, like a pregnant woman's breast,
The sky with piled clouds, covered over end to end.

SECOND STANZA OF THE DESCRIPTION OF THE RAINS
IN THE COURSE OF THE SEASONS BY THE VENERABLE KĀLIDĀSA.

ENGLISH TRANSLATION BY JOHN T. ROBERTS (1990).

Die Erforschung der klumpigen und filamentartigen Struktur interstellarer Molekülwolken ist eines der zentralen Probleme der modernen Astrophysik. Wir wissen bislang wenig über die physikalischen Prozesse, welche die Strukturierung bewirken, aber es wird vermutet, daß Turbulenz eine wesentliche Rolle spielt. In dieser Dissertation untersuche ich den Beitrag turbulenter Strömungen zur Struktur interstellarer Dunkelwolken. Dazu sind dreidimensionale numerische Hydrodynamiksimulationen notwendig, da die analytische Berechnung der detaillierten turbulenten Raum- und Geschwindigkeitsstruktur nicht möglich ist. Mit der „Lattice Boltzmann Methode“ verwende ich ein neuartiges numerisches Verfahren, bei welchem die Boltzmann-Gleichung in einem diskretisierten Phasenraum gelöst wird. Mesoskopische Teilchenpakete bewegen sich mit festen Geschwindigkeiten auf einem kartesischen Gitter und tauschen bei jedem Zeitschritt nach vorgegebenen Regeln Masse aus. Die Methode ist wegen der hauptsächlich lokalen Rechenoperationen hervorragend für die Anwendung auf Parallelrechnern oder Rechnerverbunden geeignet.

Als Teil meiner Dissertation habe ich ein parallelisiertes „Lattice Boltzmann“ Hydrodynamikprogramm entwickelt. Ich habe die numerische Stabilität der ursprünglichen Methode für Reynoldszahlen bis $10^{4.5}$ und Machzahlen bis 0.9 verbessert und das Verfahren auf zwei mischbare Phasen erweitert. Das Programm wurde auf den drei derzeit leistungsfähigsten Rechnern des Max-Planck-Instituts für Radioastronomie in Bonn sowie dem hochgradig parallelen Großrechner CM-5 der Gesellschaft für Mathematik und Datenverarbeitung in St. Augustin angewandt. Die Simulationen beinhalten kollimierte Scherströmungen und die Bewegung von Molekülwolken durch Umgebungsgas. Die Abhängigkeit der entstehenden Strukturen von der Reynoldszahl und der Machzahl werden untersucht. Die wesentlichen Ergebnisse dieser Untersuchung sind (1), daß Klumpen und Filamente nur im Übergangsbereich zwischen laminarer und voll turbulenter Strömung bei Reynoldszahlen zwischen 500 und 5000 auftreten, und (2), daß viskose *Unterschall*-scherströmungen die typische Geschwindigkeitsstruktur von Dunkelwolken hervorrufen können. Die unerwartet niedrigen Reynoldszahlen sind durch die Erhöhung der Gasviskosität durch Magnetfelder der Größenordnung $10\mu\text{G}$ und durch die enge Kopplung von ionisiertem und neutralem Gas zu erklären. Das Auftreten wohldefinierter Strukturen im Übergangsbereich zwischen hochgeordneten laminaren und chaotisch turbulenten Strömungen kann im Rahmen des Konzepts des „Edge of Chaos“ interpretiert werden. Dieser Begriff beschreibt die Tendenz komplexer Systeme nur im Bereich von Phasenübergängen zu existieren. Um die Simulationen mit Beobachtungen vergleichen zu können, habe ich mit Hilfe des 100m Radioteleskops in Effelsberg den Grundübergang von Schwefelmonoxid in Richtung der kalten Dunkelwolke L1512 kartiert. Die Daten zeigen eine Klumpenstruktur, die ich als turbulenten Schweif hinter der dichten Zentralwolke interpretiere.

Exploring the clumpy and filamentary structure of interstellar molecular clouds is one of the key problems of modern astrophysics. So far, we have little knowledge of the physical processes that cause the structure, but turbulence is suspected to be essential. In this thesis I study turbulent flows and how they contribute to the structure of interstellar dark clouds. To this end, three-dimensional numerical hydrodynamic simulations are needed since the detailed turbulent spatial and velocity structure cannot be analytically calculated. I employ the „Lattice Boltzmann Method“, a recently developed numerical method which solves the Boltzmann equation in a discretized phase space. Mesoscopic particle packets move with fixed velocities on a Cartesian lattice and at each time step they exchange mass according to given rules. Because of its mainly local operations the method is well suited for application on parallel or clustered computers.

As part of my thesis I have developed a parallelized „Lattice Boltzmann“ hydrodynamics code. I have improved the numerical stability for Reynolds numbers up to $10^{4.5}$ and Mach numbers up to 0.9 and I have extended the method to include a second miscible fluid phase. The code has been used on the three currently most powerful workstations at the „Max-Planck-Institut für Radioastronomie“ in Bonn and on the massively parallel mainframe CM-5 at the „Gesellschaft für Mathematik und Datenverarbeitung“ in St. Augustin. The simulations consist of collimated shear flows and the motion of molecular clumps through an ambient medium. The dependence of the emerging structure on Reynolds and Mach numbers is studied. The main results are (1) that distinct clumps and filaments appear only at the transition between laminar and fully turbulent flow at Reynolds numbers between 500 and 5000 and (2) that *subsonic* viscous shear flows are capable of producing the dark cloud velocity structure. The unexpectedly low Reynolds numbers can be explained by the enlargement of the gas viscosity by magnetic fields of the order $10\mu\text{G}$ and the strong coupling between ionized and neutral gas. The occurrence of well-defined structure between the highly ordered laminar and the chaotic turbulent flow regimes can be interpreted in the framework of the „Edge of Chaos“, i.e. the tendency of complex systems to exist only at the transition between phases. In order to compare the simulations with observed data I have used the 100m radio telescope at Effelsberg to map the ground transition of sulphur monoxide toward the quiescent cold dark cloud L1512. The data show a clumpy structure that I interpret as a turbulent tail behind the dense central cloud.

In dieser Arbeit gebe ich an mehreren Stellen Hinweise auf Dokumente des „World-Wide-Web¹“ (WWW). Ohne den schnellen Zugriff auf neueste Forschungsergebnisse auf dem Gebiet der „Lattice Boltzmann Methoden“, die im WWW verbreitet wurden, wäre die Entwicklung und Anwendung des parallelen Hydrodynamikprogramms im Rahmen meiner Dissertation unmöglich gewesen. Um die Arbeit einem internationalen Publikum zugänglich zu machen, habe ich mich entschlossen, sie in englischer Sprache zu verfassen und nach Abschluß auf dem WWW zur Verfügung zu stellen³.

I give pointers to “World-Wide-Web²” (WWW) documents at several places in this thesis. Without the fast access to latest research papers on “Lattice Boltzmann Methods” the development and application of the parallel hydrodynamic code would not have been possible during my Ph.D. thesis. In order to make this work accessible to an international group of researchers, I have decided to write this dissertation in English and to put it on the WWW after completion³.

¹Das World-Wide-Web ist ein hypermediales Informationssystem, das den interaktiven Zugriff auf weltweit vernetzte Rechner erlaubt. Dokumente des WWW sind durch „Uniform Resource Locator“ (URL) gekennzeichnet.

²The World-Wide-Web is a hypermedia information system that allows the interactive access to globally networked computers. WWW document addresses are given as “Uniform Resource Locators” (URLs).

³WWW-URL: <http://www.mpifr-bonn.mpg.de/iram/dmuders/dmuders.html>

Contents

1	Introduction	1
2	Lattice Hydrodynamics	7
2.1	Lattice Gas Approximation	8
2.2	Lattice Boltzmann Method	10
2.2.1	The D3Q15 Lattice	14
3	The Parallel Code	17
3.1	Numerical Stability	17
3.2	Miscible Fluid Formalism	19
3.3	Initial and Boundary Conditions	20
3.4	Parallelization	21
3.4.1	Message Passing Paradigm	22
3.4.2	Data Parallel Paradigm	22
3.4.3	ADAPTOR	24
3.5	Code Implementation	24
3.5.1	PVM/ADAPTOR Solution	26
3.5.2	CMF Solution	27
3.6	Code Performance	28
3.7	Simulation Examples	29
4	Simulations	33
4.1	Collimated Shear Flow	35
4.2	Cometary Tails	43
4.3	Results	48
5	Observations	49
5.1	Lynds 1512	49
5.1.1	Sulphur Monoxide Observations	49
5.1.2	Sulphur Monoxide Maps	50
5.1.3	Palomar Plate	51
5.2	Simulation versus Observation	57
6	Summary and Conclusion	59
	Bibliography	61

List of Figures

1.1	<i>Carbon Monoxide Maps of the Cloud Hierarchy in TMC-1</i>	2
1.2	<i>Artificial Clump Hierarchy Resembling Interstellar Clouds</i>	4
1.3	<i>Artificial Clump Hierarchy Resembling Terrestrial Clouds</i>	5
2.1	<i>The FHP Lattice</i>	9
2.2	<i>The D3Q15 Lattice</i>	15
3.1	<i>Two-Phase Diffusion Experiment</i>	20
3.2	<i>The CM-5 Parallel Supercomputer</i>	23
3.3	<i>General Program Structure</i>	25
3.4	<i>Data Distribution under PVM</i>	27
3.5	<i>Turbulent Flow around a Hard Sphere</i>	30
3.6	<i>Time Development of a Cylinder Wake</i>	31
4.1	<i>Column Density of a Shear Flow with $Re=200$, $Ma=0.6$</i>	35
4.2	<i>Time Sequence of a Shear Flow with $Re=1000$, $Ma=0.9$</i>	37
4.3	<i>3D Volume Rendering of a Shear Flow with $Re=1500$ and $Ma=0.9$</i>	39
4.4	<i>Model Spectra of a Shear Flow with $Re=1000$ and $Ma=0.9$</i>	41
4.5	<i>Column Density of a Shear Flow with $Re=20000$ and $Ma=0.6$</i>	41
4.6	<i>Model Spectra for a Shear Flow with $Re=20000$, $Ma=0.6$</i>	42
4.7	<i>Time Sequence of a Developing Pulsating Instability</i>	44
4.8	<i>3D Volume Rendering of a Pulsating Cometary Tail</i>	45
4.9	<i>Model Spectra of a Cometary Tail with $Re=3000$ and $Ma=0.6$</i>	45
4.10	<i>3D Volume Rendering of the Turbulent Cometary Tail behind Three Clumps</i>	47
5.1	<i>L1512 SO $1_0 - 0_1$ Spectra</i>	52
5.2	<i>L1512 Integrated SO Intensity</i>	53
5.3	<i>L1512 Channel Maps</i>	54
5.4	<i>L1512 True Color Plot</i>	55
5.5	<i>Red Palomar Plate toward L1512</i>	56
5.6	<i>Model Sulphur Monoxide Spectra</i>	58

List of Tables

2.1	<i>D3Q15 Equilibrium Coefficients to Second Order in Velocity</i>	14
3.1	<i>D3Q15 Equilibrium Coefficients to Fourth Order in Velocity</i>	18

Chapter 1

Introduction

Nature provides us with a fascinating variety of self-organizing systems where often a simple microscopic rule leads to surprisingly complex, sometimes self-similar macroscopic structures. A well-known example is the continuous bifurcation of branches which produces the typical look of plants such as trees, etc. Generally, the development of ordered textures, instead of totally random chaos, is caused by the competition between nonlinear growth and corresponding dissipative forces. This leads to the amplification or slaving of only a few basic modes which then represent the macroscopic pattern that we observe (see e.g. Haken 1983). A classic example of this kind is the formation of hexagonal prismatic Bénard cells in a fluid layer heated from below. Here, the growth of higher than the first three convective modes is inhibited by the temperature dependence of the fluid viscosity.

The situation in these simple systems is rather clear-cut. In many cases, however, it is not easy to understand how the observed patterns have evolved. One of the most interesting astronomical examples is the spatial and velocity structure of interstellar clouds, the birthplaces of new stars. These clouds consist of a gaseous and a dust phase. The gas contains mainly molecular hydrogen (H_2) at average densities of $10^2 - 10^3 \text{ cm}^{-3}$ with a small mass fraction ($< 10^{-3}$) of numerous tracer gases like carbon monoxide (CO), ammonia (NH_3), sulphur monoxide (SO), etc. Although dynamically seen the molecular hydrogen is the most important cloud ingredient, we cannot directly observe it. At the low cloud temperatures of 10 – 100 K only rotational energy states are excited by molecule collisions. But H_2 does not have a permanent dipole moment so that it does not emit radiation. The tracer molecules, on the other hand, do emit line radiation which can be observed with radiotelescopes. However, deriving the H_2 distribution from these measurements is complicated since there may be varying molecule abundances or excitation conditions.

The clouds' dust phase is believed to consist of graphite and silicates grains (see e.g. Mathis et al. 1977) which absorb short wavelength photons like the ultraviolet emission of stars and reemit millimeter to infrared continuum radiation. Thus, the dust causes the dark patterns on optical plates which coined the name "*dark clouds*". Dust grains play an important role in dark cloud chemistry. Apart from direct two-atom gas reactions, molecules are synthesized on the dust grain surfaces. Atoms hit the grains, stick to them and react while the binding energy is taken by the grain's lattice. The new molecule may then be thermally evaporated into the gas phase.

Observations of dark molecular clouds reveal a very complex clumpy and filamentary structure. Clumps are seen on spatial scales spanning several orders of magnitude from giant molecular clouds to protostellar environments (see e.g. maps in Figure 1.1). The lineshapes

often exhibit multiple peaks and non-gaussian wings. So far, there is no conclusive model for the origin of interstellar cloud structure. To tackle the problem, first, a number of phenomenological descriptions have been sought by different authors. Stutzki and Güsten (1990), for example, proposed to decompose spectral maps into Gaussian clumps and to determine the size and mass distributions. For the M17 SW cloud core they found the number of clouds (dN) per mass interval (dM) to be proportional to $M^{-1.7 \pm 0.15}$.

Similar studies have been carried out by Williams and Blitz (1993) and Williams et al. (1994). Their “CLUMPFIND” algorithm has been applied to maps of the star forming Rosette molecular cloud (RMC) and to the quiescent Maddalena molecular cloud (MMC) (Maddalena and Thaddeus 1985). The respective relations are $(dN/dM)_{RMC} \sim M^{-1.32}$ and $(dN/dM)_{MMC} \sim M^{-1.44}$. Thus, within statistical errors, there seems to be no significant difference between regions exhibiting stars formation activity and those containing quiescent clouds. The reason for this may be that the quiescent regions, like the MMC, are in an intermediate state where their clumpiness has just been inherited from past star formation activity. But upon examining the MMC’s far-infrared emission, which is believed to be re-radiated star light, one finds that it is two orders of magnitude lower than the value derived for typical star forming giant molecular clouds (GMCs) (Blitz 1993; Boulanger and Pérault 1988). Thus, the Maddalena cloud really seems to be in a primordial phase. The similar clumpy structure that we observe in the star forming and quiescent clouds might therefore be generated by physical processes common to both.

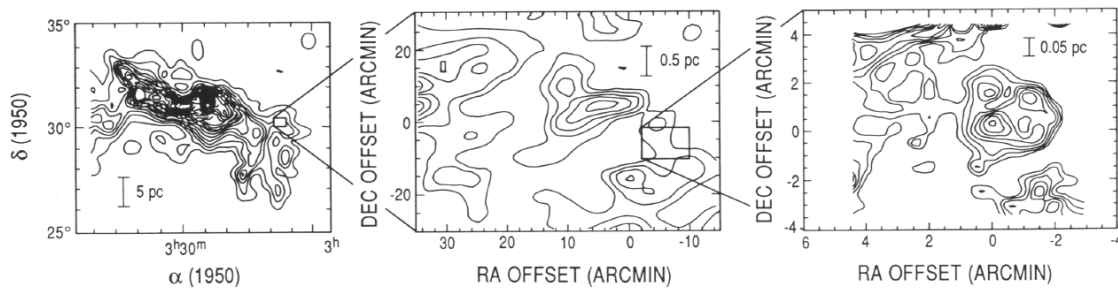


Figure 1.1: *Interstellar clouds are among the most interesting astronomical examples of self-organizing systems. The above example shows maps on three different length scales of a region in the “Taurus Molecular Cloud 1” (TMC-1) (from: Ungerechts and Thaddeus 1987 and Falgarone et al. 1991). The contours denote velocity integrated radio emission from carbon monoxide molecules. Self-similar, hierarchical cloud complexes are visible over two orders of magnitude in length.*

By applying other measures of complexity one can try to find out more about the nature of the relevant physical processes. Houllahan and Scalo (1992) have found evidence for self-similar, hierarchical structure in molecular clouds. They classified the spatial order of isophotes, contours of equal intensity, in the form of “structure trees” and compared them with theoretical maps. Langer et al. (1993) used Laplacian pyramid transforms, a special form of nonorthogonal wavelets, to analyze the hierarchical structure.

In fact, the observed structures can be quite easily reproduced by simple hierarchical models. Figure 1.2 shows an example where I have calculated an artificial column density map of a 3D hierarchy of clouds. First, 10 large clumps with Gaussian density profile have been randomly placed into a cube volume. Then, 10 Gaussian clumps with half the initial size have been placed *into each* of the first clumps. Again, 10 smaller clumps have been put into the second generation clumps. Repeating this algorithm for a couple of times a typical

“astronomical” map can be generated. Similar results have been published by Hetem and Lépine (1993). It is important to note that the same model can be used for terrestrial clouds. Just increasing the number of small Gaussian clumplets leads to the typical fuzzy shape of atmospheric clouds (see Figure 1.3). The similarity between both cases leads to the speculation that there might be similar physical causes for both the atmospheric and the interstellar cloud structure. The morphological resemblance was, of course, the reason for coining the name “Interstellar Clouds”.

More evidence for a physical connection between both cases comes from the measurement of the fractal or Hausdorff dimension D of isophotes in both cases. D describes the contours’ “wrinkledness”. The fractal dimension is defined by $L \sim A^{\frac{D}{2}}$ where L is the isophote’s length and A is the area enclosed by the contour. Lovejoy (1982) evaluated radar maps of rain clouds. He finds $D_{rain\ clouds} = 1.35 \pm 0.05$. Falgarone et al. (1991) did the same thing for IRAS, carbon monoxide and H I maps of different interstellar clouds. They obtained an average of $D_{i.s.clouds} \approx 1.4$. Both D values are rather close to the fractal dimension $D_{turb.} = \frac{4}{3}$ for the case of homogeneous isotropic Kolmogorov turbulence (Falgarone and Phillips 1990).

In a recent paper Falgarone et al. (1994) compare the synthetic spectra from a 3D simulation of decaying compressible isotropic turbulence with carbon monoxide observations of a quiescent cloud in Ursa Majoris. They find that turbulence at Mach numbers around unity without strong shocks can reproduce the general *spectral* features observed toward molecular clouds. However, their isotropic model cannot account for the observed spatial clumpiness. Nevertheless, it seems ingenious to include turbulent flows into a model for the interstellar cloud structure. But it is still an open question as to which processes are mainly involved in producing the turbulent velocity field. Star forming regions contain numerous possible energy sources like bipolar outflows, stellar winds, ejecta from planetary nebulae and/or supernovae. Gravitation and magnetic fields may play an important role in some parts of the clouds. It is difficult to predict the relative importance of the individual contributions, so a realistic model should include all processes.

The situation is much clearer for the more quiescent regions of the interstellar medium. These relatively unperturbed and often isolated cold dark clouds exhibit similar spatial and velocity structure but lack the diversity of energetic processes which accompany ongoing star formation. The only remaining source of energy is the motion of these clouds through the ambient medium. The resulting shear forces might cause the observed structure via instabilities of Kelvin-Helmholtz type. It seems feasible to first try to model such flows and to explore the structure of cold clouds. Later, one should proceed toward a global model of the interstellar medium.

The main focus of this thesis work is to numerically investigate basic turbulent dark cloud shear flows with respect to their contribution to spatial and velocity structure. The model must be three-dimensional to account for the observed anisotropic morphologies and to allow the calculation of artificial spectra for comparison with molecular line data. The numerical method must be able to simulate flow velocities on the order of the sound speed. To simulate turbulent flows the possible Reynolds numbers should be well above the classical critical value of roughly $Re = 2000$. The algorithm must be flexible enough to easily implement the basic ingredients of the interstellar medium (hydrogen, tracer molecules, dust grains) and allow future extensions like multicomponent models with chemical reactions, inclusion of magnetic fields, etc. It should be applicable on massively parallel computers since this is currently the only way to get sufficient computational performance and ample spatial resolution in three dimensions.

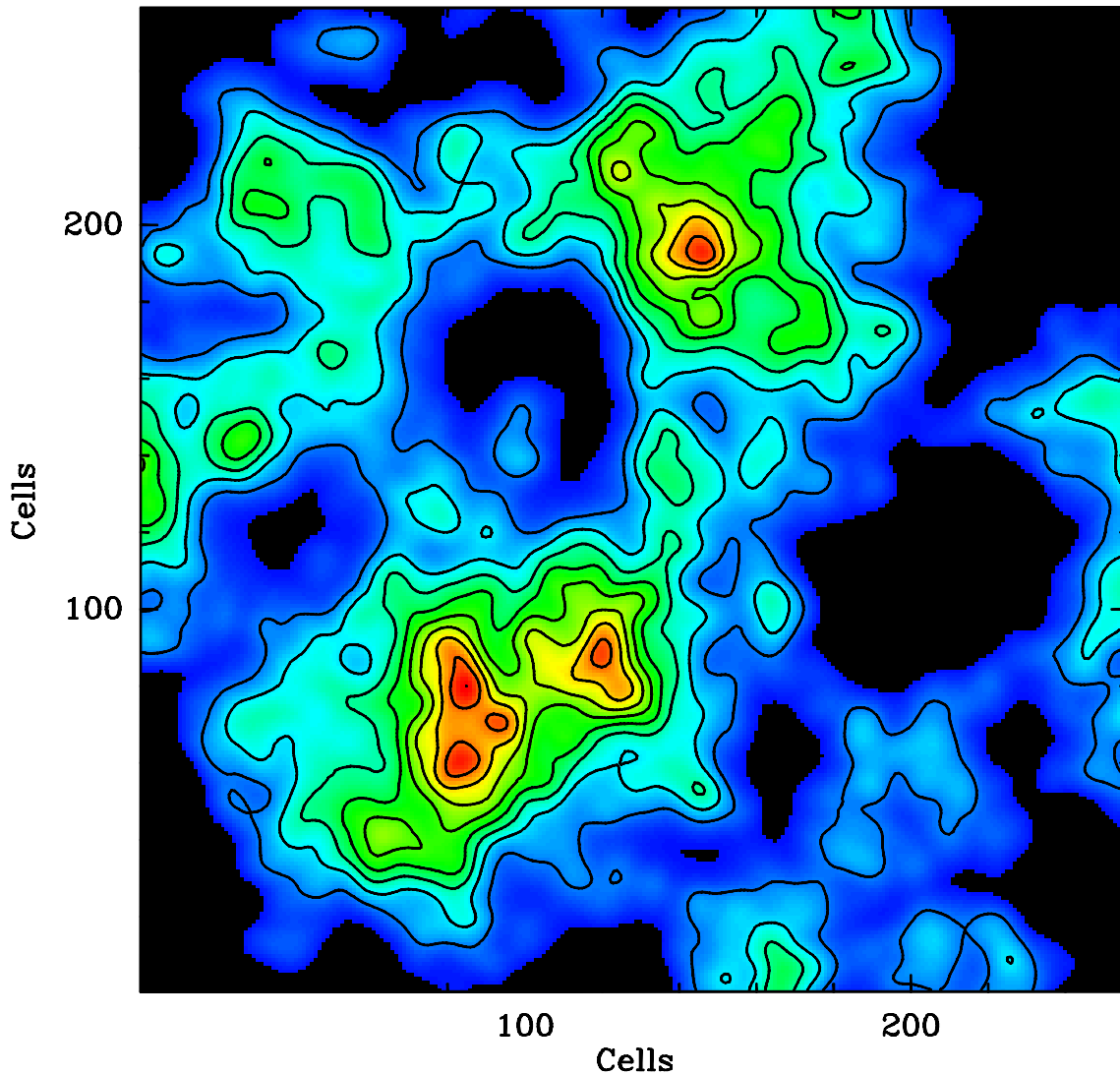


Figure 1.2: Using a simple hierarchical distribution of clumps with Gaussian density profile where the smaller clumps lie within the larger ones, it is easy to produce maps that strongly resemble astronomical data (compare to Figure 1.1). In this example 10 initial clumps of 128 pixel diameter have been randomly placed onto a square of 256^2 pixels. Ten clumps with half the initial size have been placed into each of the initial clouds. Again, 10 smaller clumps have been put randomly into the second generation clouds and so on. Thus, 5 generations of subclumps have been produced. Although this phenomenological approach is working fairly well, the physical processes which produce such a hierarchy of clumps still remain to be determined.

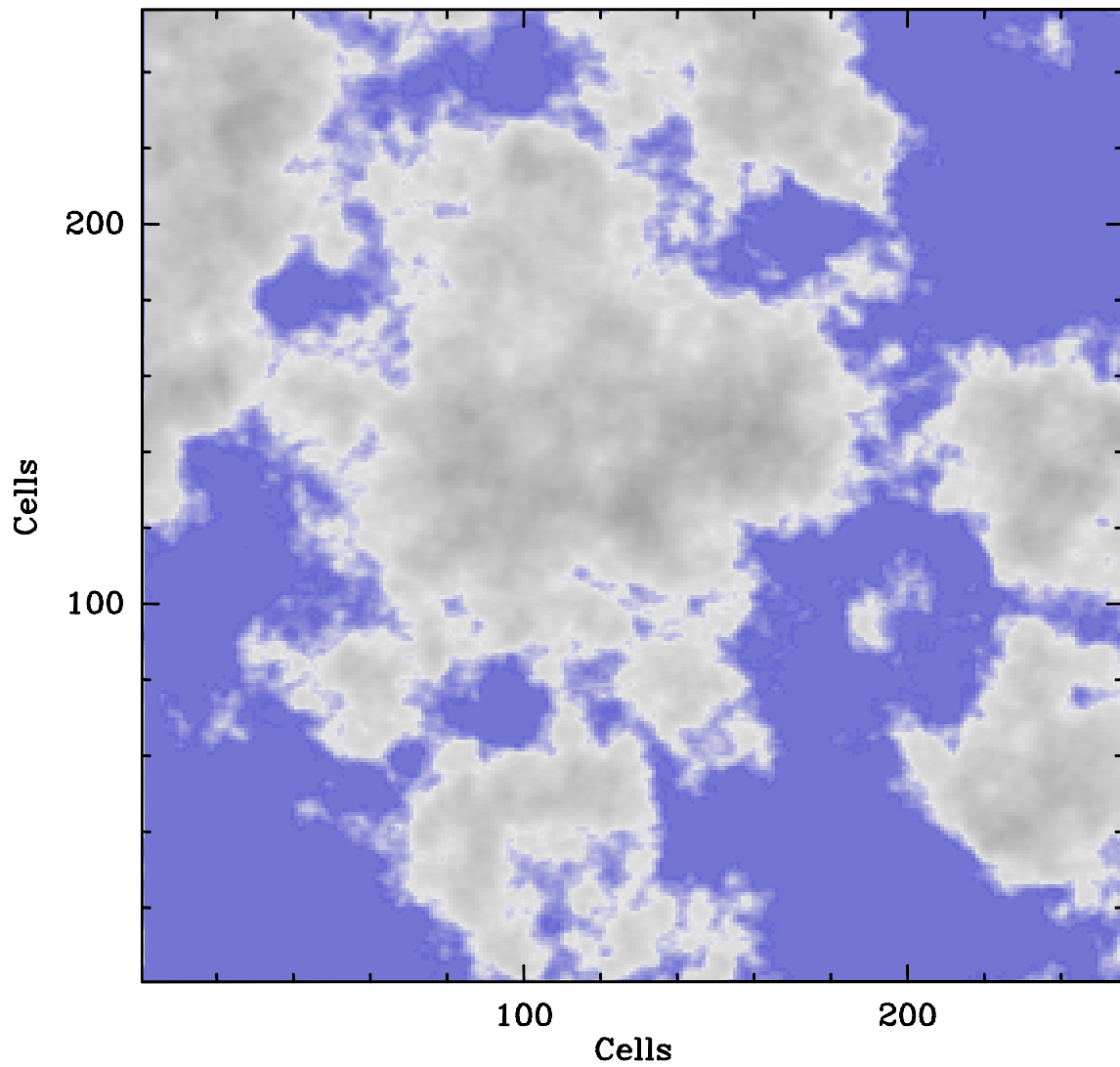


Figure 1.3: Using the same hierarchical model as for the interstellar clouds it is straightforward to also model terrestrial clouds. Only the number of smaller cloudlets has been increased to get the typical fuzzy shape. The similarity between both cases leads to the assumption that similar physical processes might control the evolution of atmospheric clouds and their interstellar counterparts.

In this dissertation I will introduce the recently developed “Lattice Gas” (LG) and “Lattice Boltzmann” (LB) methods as new tools to meet all these requirements. In these hydrodynamical models the microscopic gas structure is represented by particles or particle packets which move with *discrete* velocities on a regular lattice. Due to only local collisional particle interactions the methods are extremely well suited for distributed computing and they can easily include “objects” of arbitrarily complex shape like interstellar dust clouds. As far as I know this is the first time that an LG/LB method has been applied to an astrophysical problem.

As part of my thesis I have developed and tested the basic numerical “Lattice Boltzmann” code and the necessary extensions for simulating interstellar flows. I have parallelized the program for the cluster of workstations at the Max-Planck-Institut für Radioastronomie (MPIfR⁴) in Bonn and for the CM-5 parallel supercomputer at the GMD⁵ in St. Augustin. With both parallel codes I have carried out a systematic investigation of different dark cloud shear flows by considering the dependence of the emanating structures on Mach and Reynolds numbers.

To provide an observational example for the comparison with the simulations, I have mapped the cold dark cloud L1512 (Lynds 1962) with the MPIfR 100m radiotelescope at Effelsberg. L1512 is a very quiescent cloud which does not exhibit any sign of massive star formation. Using continuous scanning (“On-The-Fly”) and frequency switching techniques, I have obtained a fully sampled map of the ground rotational transition of sulphur monoxide, a molecule which proved to be a tracer of extended dark cloud structures not seen with other molecular transitions (Schmid-Burgk and Muders 1994).

⁴WWW-URL: <http://www.mpifr-bonn.mpg.de>

⁵Gesellschaft für Mathematik und Datenverarbeitung mbH / Forschungszentrum Informationstechnik GmbH; German National Research Centre for Mathematics and Computer Science / German National Research Center for Information Technology; WWW-URL: <http://www.gmd.de>

Chapter 2

Lattice Hydrodynamics

In computational fluid dynamics (CFD) one traditionally tries to integrate the macroscopic partial differential equations of hydrodynamics, i.e. the Navier-Stokes equations (see e.g. Landau and Lifschitz 1966)

$$\begin{aligned}\frac{\partial \rho}{\partial t} + \operatorname{div}(\rho \vec{v}) &= 0 \\ \frac{\partial \vec{v}}{\partial t} + (\vec{v} \nabla) \vec{v} &= -\frac{\nabla p}{\rho} + \nu \Delta \vec{v} + \left(\frac{\zeta}{\rho} + \frac{\nu}{3}\right) \nabla \operatorname{div}(\vec{v}) \quad .\end{aligned}\tag{2.1}$$

With the advent of larger and faster computers it has become feasible to leave the continuum description and to go back to the simpler microscopic model of kinetic gas theory. This theory had been suggested as early as 1738 by Bernoulli to explain gas pressure and had later been refined by Maxwell (1860) and Boltzmann (1868).

The new microscopic computational models simulate individual particles which move with *discrete* velocities on a regular lattice. Lattice methods are perfectly suited to run on parallel or distributed computers, a technology which is becoming more and more important since it provides, at rather low expenses, much better performance than single CPU systems.

It is important to note that lattice methods are closely related to “Cellular Automata” (see e.g. Wolfram 1986). Those are systems of cells in given states that evolve in time. A cell’s state changes depending on the conditions in the neighboring cells only. Cellular automata may produce extremely complex structures from the evolution of rather simple *local* rules. One famous example is Conway’s “Life” (Conway 1968) where, on a 2D grid, cells are either “dead” or “alive”. In one timestep the cell’s fate is dependent on the number of “living” neighboring cells. If that number exceeds or falls short of given limits, then the central cell dies, otherwise it survives or a new cell is generated. Upon letting this algorithm work on random initial conditions for a couple of timesteps, it always selects the same few stable configurations.

Fluid motion is a similar self-organizing process evolving from the microscopic collisions of atoms or molecules. This microstructure is simulated by the lattice methods so that they may provide a better numerical tool to tackle longstanding hydrodynamical problems, especially turbulent flow. I have therefore developed a parallel code based on hydrodynamic lattice theory to explore dark cloud flows. In this chapter I will briefly describe the historical development of lattice methods from the “Lattice Gases” to the “Lattice Boltzmann Methods”. I will give the explicit derivation of the latter models which I have used to simulate viscous, compressible fluid flows.

2.1 Lattice Gas Approximation

The “Lattice Gas Approximation” (LGA) is the earliest new microscopic CFD approach. A two-dimensional LGA model was first proposed in the early seventies (Hardy and Pomeau 1972; Hardy et al. 1973, 1976). In the LGA individual particles of equal mass move in discrete time steps on a lattice. Each particle is assigned a fixed velocity along one of the links to neighboring cells. A time step consists of two actions: free streaming and collision. First, all particles are moved to neighboring cells along the lattice links according to their microscopic velocity. Then they collide under conservation of particle number, energy and momentum. The explicit collision rules determine the viscosity of the system. For computational efficiency all LGA models assume Fermi-like statistics, i.e. only one particle per discrete velocity is allowed at each lattice node. For a large number of particles the macroscopic behavior of such an “atomic level” model is that of an incompressible fluid or a gas in the low Mach number limit.

Due to its microscopic approach the LGA method has a number of computational advantages. It is ideally suited for the use on parallel or distributed computers because most operations are local. Complicated flow geometries, including hard objects of arbitrary shape are easily realized since interactions with obstacles can be represented by simple particle bouncing. “Lattice Gases” are absolutely stable because no floating point calculations are involved. The discrete velocities are coded by single bits so that on today’s computers rather large numbers of particles ($> 10^8$) may be simulated. The macroscopic floating point quantities like density, velocity etc. are calculated only at the end of a simulation by averaging the populations over a sufficiently large number of grid cells.

Apart from the purely hydrodynamic models, the “Lattice Gas” method has also been applied to a wide field of other problems like thermo-hydrodynamics (Bagnoli et al. 1993), magneto-hydrodynamics (Chen et al. 1992; Montgomery and Doolen 1987), radiation transport (Nickel 1988), immiscible fluids with surface tension (Adler et al. 1994; Rothman and Keller 1988), liquid-gas flow (Appert and Zaleski 1993; Chen et al. 1989) and reaction-diffusion systems (Chopard et al. 1993; Lawniczak and collaborators 1991). A more complete overview of LGA can be found in a review by Boghosian (1993). Most of the information that was needed to design the models for this thesis came from the Los Alamos preprint server⁶, which stores recent papers on “Lattice Gas” research with full text and often with included figures. Thus, the “World-Wide-Web” concept (see footnote 2) proved to be extraordinarily useful to me.

The first hydrodynamical LGA model by Hardy and collaborators (*loc. cit.*) employed a Cartesian square lattice. The resulting macroscopic hydrodynamic equations proved to be anisotropic. Later, Frisch, Hasslacher and Pomeau (FHP, 1986) showed that in two dimensions a lattice with $\frac{\pi}{3}$ symmetry, i.e. a triangular lattice, must be used to ensure isotropy. Each cell has six nearest neighbors and consequently six possible velocity directions. The geometrical outline of this model is shown in Figure 2.1. The FHP model became the first really usable two-dimensional “Lattice Gas” and has since been used and extended by many authors.

Because of the isotropy requirement the construction of three-dimensional models is not as straightforward as one might expect. In the 3D case a lattice with icosahedral symmetry is needed (Wolfram 1986). Unfortunately there is no regular 3D lattice with this symmetry. D’Humières et al. (1986) proposed to use the 3D projection of the four-dimensional face-centered hypercube (4D FCHC). This lattice consists of the 24 nodes $\{(\pm 1, \pm 1, 0, 0), (\pm 1, 0, \pm 1, 0), (\pm 1, 0, 0, \pm 1), (0, \pm 1, \pm 1, 0), (0, \pm 1, 0, \pm 1), (0, 0, \pm 1, \pm 1)\}$.

⁶WWW-URL: gopher://xyz.lanl.gov/11/comp-gas

The 4D FCHC lattice provided the base for a working 3D model. However, now each particle has 24 neighbors and therefore the number of possible collisions is much higher than in the 2D FHP model (2^{24} compared to 2^6). If all collisions are mapped explicitly in a numerical code, then 48 MByte of memory are needed. This drastically reduces the space for the data cube itself even on current computer systems.

A way out of this dilemma is the reduction of the collision table by systematic algorithms. Hénon proposed to use only collisions that are isometries between the initial and the final states (Hénon 1987). His method reduces the number of rules from 2^{24} to 302209, which is roughly 2% of the original size. On one hand this improves the computational efficiency very much, but on the other hand the new isometric collision rules set a lower limit on the viscosity so that only flows with rather low Reynolds numbers can be simulated. Therefore much research has been devoted to find the optimal collision rules (see e.g. Dubrulle et al. 1990). A good improvement has been obtained by Somers and Rem (1989) who used smaller lookup tables that are applied to subsets of the full 24 bit input states.

The FHP lattice

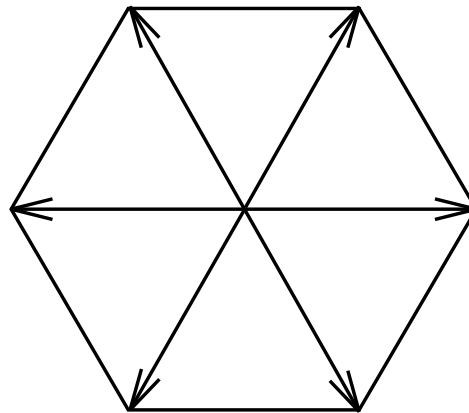


Figure 2.1: *The hexagonal structure of the FHP “Lattice Gas” model proposed by Frisch et al. (1986). Six discrete velocity directions are allowed at each lattice node. The FHP model was the first working 2D method and has since been used and developed by many authors.*

But even with the best collision rules so far, the possible range of Reynolds numbers in LGA simulations is still too low for simulating turbulent flows. Additionally, LGA simulations are restricted to only incompressible fluid flow due to the lack of Galilean invariance and the subsequent need of a linear macroscopic rescaling. Finally, the discretization noise, inherent in LGA models, requires averaging over a large number of grid cells so that the spatial resolution is reduced.

A solution to all these problems was found by the development of the “Lattice Boltzmann Method” (LBM) (see e.g. McNamara and Zanetti 1988; Higuera and Succi 1989; Higuera and Jiménez 1989) as alternative numerical tool. It is noise-free and can be used for the simulation of turbulence. The LBM retains most of the computational advantages of the LGA models except for the absolute numerical stability because it is partly a floating point algorithm.

2.2 Lattice Boltzmann Method

The LBM simulates the evolution of ensemble averaged distributions f_{qi} instead of the discrete particles that have been used in the LGA case. The f_{qi} are allowed to take any real value so that the Fermi-like statistics no longer apply. The indices qi describe the D -dimensional sub-lattices defined by the permutations of $(\pm 1, \dots, \pm 1, 0, \dots, 0)$ where q is the number of non-zero components and i counts the sub-lattice vectors. The corresponding packet velocities will be denoted by \vec{c}_{qi} . Note that in contrast to the LGA models, “rest particles” with zero velocity are allowed. They are essential for simulating compressible hydrodynamics via a tunable model sound speed (Chen et al. 1993). Chen et al. have given a general formalism for D -dimensional LBMs. I have used important parts of Chen’s work. In the subsequent derivations I will therefore employ a notation similar to theirs.

Again, for the LBM space, time and particle packet velocities are discretized. The time evolution of the system is governed by the Boltzmann equation in discrete phase space

$$f_{qi}(\vec{r} + \vec{c}_{qi}\Delta t, t + \Delta t) - f_{qi}(\vec{r}, t) = \Omega_{qi} \quad . \quad (2.2)$$

The term $\vec{r} + \vec{c}_{qi}\Delta t$ describes the propagation of the particle packets along the lattice links. It is convenient to set $\Delta t = 1$ to get a scale-free model formalism. Ω is a general collision operator. The collisions are again completely local so that the LBM is, like the LGA, very efficiently parallelizable.

The macroscopic variables density (ρ) and velocity (\vec{v}) follow from the respective velocity moments of the particle distributions

$$\begin{aligned} \rho &= \sum_{qi} f_{qi} \\ \vec{v} &= \frac{1}{\rho} \sum_{qi} f_{qi} \vec{c}_{qi} \quad . \end{aligned} \quad (2.3)$$

These quantities should be conserved in the collisional phase. Therefore the velocity moments of the collision term Ω must vanish

$$\begin{aligned} \sum_{qi} \Omega_{qi} &= 0 \\ \sum_{qi} \Omega_{qi} \vec{c}_{qi} &= \vec{0} \quad . \end{aligned} \quad (2.4)$$

The first LBM models used a form of Ω that was the direct transcription of the LGA method, i.e. complete particle packets are exchanged between different lattice directions without altering their mass content (McNamara and Zanetti 1988). By using this approach the particles’ mean free path and thus the fluid viscosity are still fixed. Releasing that constraint and allowing matter exchange between the packets leads to variable viscosity (Higuera and Jiménez 1989). In this case Ω is a general $(q \cdot i) \times (q \cdot i)$ matrix.

The collision term may be linearized assuming that there is always a *local* equilibrium particle distribution f_{qi}^{eq} dependent on the conserved quantities ρ and \vec{v} only. To first order one gets

$$\Omega_{qi}(f_{qi}) = \Omega_{qi}(f_{qi}^{eq}) + \Omega'_{qi}(f_{qi} - f_{qi}^{eq}) \quad (2.5)$$

where “eq” denotes equilibrium values. To ensure the local conservation of mass and momentum the equilibrium distributions must satisfy

$$\begin{aligned} \sum_{qi} f_{qi}^{eq} &= \sum_{qi} f_{qi} \\ \sum_{qi} f_{qi}^{eq} \vec{c}_{qi} &= \sum_{qi} f_{qi} \vec{c}_{qi} \quad . \end{aligned} \quad (2.6)$$

Since Ω now only acts on the departures from equilibrium the first term in equation 2.5, namely $\Omega(f_{qi}^{eq})$, vanishes. The simplest and computationally most efficient form of Ω'_{qi} is a relaxation of “Bhatnagar-Gross-Krook” (BGK) type (Bhatnagar et al. 1954). Defining $\Omega'_{qi} \equiv -\omega := -\frac{1}{\tau}$, $\forall i$ the discrete Boltzmann-BGK equation reads

$$f_{qi}(\vec{r} + \vec{c}_{qi}, t + 1) = f_{qi}(\vec{r}, t) - \frac{1}{\tau} \left(f_{qi}(\vec{r}, t) - f_{qi}^{eq}(\rho, \vec{v}) \right) . \quad (2.7)$$

The BGK relaxation gives maximal local randomization. All particle distributions f_{qi} relax with the same rate ω on the timescale τ toward their corresponding equilibrium value. The relaxation rate must obey $0 < \omega < 2$ for the method to be linearly stable and for the particle density to be positive (Qian et al. 1992). The condition where $0 < \omega < 1$ is called subrelaxation while $1 < \omega < 2$ means overrelaxation. It has been shown by Behrend et al. (1993) that the BGK simplification of the collision operator is a good approximation and that the additional freedom of the full LBM matrix does not improve the method. For higher Reynolds numbers the BGK method performs even better (Succi et al. 1993). Since the BGK model is also computationally advantageous it has become the main tool for LBM simulations. Therefore it has also been used for the simulations presented in this thesis.

It now remains to specify an expression for the equilibrium distributions which is dependent on the conserved quantities only. There is considerable freedom in the choice of f_{qi}^{eq} . A general parametrized form is the Taylor's series of a lattice Maxwell-Boltzmann distribution

$$f_{qi}^{eq}(\rho, \vec{v}) = \rho \left(A_q + B_q(\vec{c}_{qi}\vec{v}) + C_q\vec{v}^2 + D_q(\vec{c}_{qi}\vec{v})^2 + \dots \right) . \quad (2.8)$$

The coefficients A_q to D_q are dependent on the employed lattice geometry. For hydrodynamic models they are constant. In case of thermo-hydrodynamic models they additionally depend on the thermal energy (see e.g. Chen et al. 1994). In this thesis I have used a purely hydrodynamic model since my test simulations showed that the numerical stability of all current 3D thermo-hydrodynamic “Lattice Boltzmann Models” (Alexander et al. 1993; McNamara and Alder 1993; Qian 1993; Chen et al. 1994) is not yet good enough for simulating interstellar flows. I also did not use the additional constant which had been introduced into the equilibrium distributions by different authors (see e.g. Chen et al. 1993). This was originally done to avoid negative f_{qi} values but in fact it decreases the numerical stability especially for low viscosity and high Mach number.

The equilibrium distributions must be chosen such, that for each given lattice the Navier-Stokes equations emerge macroscopically. First, some lattice specific relations have to be noted. The first four tensors of lattice velocity moments are defined as follows

$$\begin{aligned} T_{q\alpha} &= \sum_i c_{qi\alpha} &= 0 \\ T_{q\alpha\beta} &= \sum_i c_{qi\alpha} c_{qi\beta} &= \frac{b_q q}{D} \delta_{\alpha\beta} \\ T_{q\alpha\beta\gamma} &= \sum_i c_{qi\alpha} c_{qi\beta} c_{qi\gamma} &= 0 \\ T_{q\alpha\beta\gamma\delta} &= \sum_i c_{qi\alpha} c_{qi\beta} c_{qi\gamma} c_{qi\delta} &= \psi_q \gamma_{\alpha\beta\gamma\delta} + \varphi_q (\delta_{\alpha\beta} \delta_{\gamma\delta} + \delta_{\alpha\gamma} \delta_{\beta\delta} + \delta_{\alpha\delta} \delta_{\beta\gamma}) \end{aligned} \quad (2.9)$$

where $b_q = \frac{2^{q+1} D}{q!(D-q)!}$ is the number of base vectors in a sub-lattice and $\delta_{\alpha\beta}$ and $\gamma_{\alpha\beta\gamma\delta}$ are the respective Kronecker symbols in 2 and 4 dimensions. The lattice dependent functions ψ_q and φ_q may be calculated according to Qian (1990) by

$$\psi_0 := 0, \quad \varphi_0 := 0 \quad \text{and} \quad \left. \begin{aligned} \psi_q &= \frac{(D+2-3q)b_q q^2}{qD(D-1)} \\ \varphi_q &= \frac{(q-1)b_q q^2}{qD(D-1)} \end{aligned} \right\} \forall q > 0 . \quad (2.10)$$

To get macroscopically isotropic equations it is required that

$$\sum_q t_q \psi_q = 0 \quad (2.11)$$

where t_q denotes the fraction of ρ on sub-lattice q . With the abbreviation $\sigma = \frac{D}{\sum_q t_q b_{q,q}}$ the equilibrium coefficients for the rest particles are defined by

$$\begin{aligned} A_0 &= t_0 \\ B_0 &= 0 \\ C_0 &= - \left[\frac{1 - \sigma^2 (1 - t_0 b_0) \sum_q t_q \varphi_q}{2\sigma \sum_q t_q \varphi_q} \right] \\ D_0 &= 0 \end{aligned} \quad (2.12)$$

and for the moving particles by

$$\begin{aligned} A_q &= t_q \\ B_q &= t_q \sigma \\ C_q &= -t_q \frac{\sigma}{2} \\ D_q &= t_q \frac{1}{2 \sum_q t_q \varphi_q} . \end{aligned} \quad (2.13)$$

To finally derive the continuum description and the transport coefficients from the discrete Boltzmann equation in the long wavelength and low frequency limits one first expands equation 2.7 into a Taylor's series. Assuming implicit sums over multiple Cartesian components indexed by Greek subscripts one gets to second order

$$\partial_t f_{qi} + c_{qi\alpha} \partial_\alpha f_{qi} + \frac{1}{2} \partial_t^2 f_{qi} + c_{qi\alpha} \partial_t \partial_\alpha f_{qi} + \frac{1}{2} c_{qi\alpha} c_{qj\beta} \partial_\alpha \partial_\beta f_{qi} = -\frac{1}{\tau} (f_{qi} - f_{qi}^{eq}) . \quad (2.14)$$

Then a multi-scale Chapman-Enskog perturbative expansion is applied to the particle distributions and the time and space derivatives via

$$\begin{aligned} f_{qi} &\rightarrow f_{qi}^0 + \varepsilon f_{qi}^1 \\ \partial_t &\rightarrow \varepsilon \partial_{t_1} + \varepsilon^2 \partial_{t_2} \\ \partial_\alpha &\rightarrow \varepsilon \partial_\alpha . \end{aligned} \quad (2.15)$$

$f_{qi}^0 \equiv f_{qi}^{eq}$ so that the integrals over the perturbation term f_{qi}^1 must vanish

$$\begin{aligned} \sum_{qi} f_{qi}^1 &= 0 \\ \sum_{qi} \vec{c}_{qi} f_{qi}^1 &= \vec{0} . \end{aligned} \quad (2.16)$$

Equation 2.15 is now used to replace the respective terms in equation 2.14. Retaining terms on first order of ε gives

$$\partial_{t_1} f_{qi}^0 + c_{qi\alpha} \partial_\alpha f_{qi}^0 = -\frac{1}{\tau} f_{qi}^1 . \quad (2.17)$$

Integration of this equation and its velocity moment over the discrete velocity space and using the definitions from equations 2.3 and 2.9 leads to the following macroscopic relations

$$\begin{aligned} \partial_{t_1} \rho + \partial_\alpha (\rho v_\alpha) &= 0 \\ \partial_{t_1} (\rho v_\alpha) + \partial_\beta (\rho v_\alpha v_\beta) &= -\frac{1}{\sigma} \partial_\alpha \rho . \end{aligned} \quad (2.18)$$

Examining the terms on second order of ε one gets

$$\partial_{t_1} f_{qi}^1 + c_{qi\alpha} \partial_\alpha f_{qi}^1 + \partial_{t_2} f_{qi}^0 + \frac{1}{2} \partial_{t_1}^2 f_{qi}^0 + c_{qi\alpha} \partial_{t_1} \partial_\alpha f_{qi}^0 + \frac{1}{2} c_{qi\alpha} c_{qj\beta} \partial_\alpha \partial_\beta f_{qi}^0 = 0 \quad . \quad (2.19)$$

Again, integrating this result over the discrete velocity space produces another two macroscopic equations

$$\begin{aligned} \partial_{t_2} \rho &= 0 \\ \partial_{t_2} (\rho v_\alpha) + \left(\tau - \frac{1}{2}\right) \frac{1}{\sigma} \partial_\alpha [\partial_\gamma (\rho v_\gamma)] \\ - \left(\tau - \frac{1}{2}\right) \sum_q (t_q \varphi_q) \sigma \partial_\beta [\partial_\gamma (\rho v_\gamma) \delta_{\alpha\beta} + \partial_\alpha (\rho v_\beta) + \partial_\beta (\rho v_\alpha)] &= 0 \quad . \end{aligned} \quad (2.20)$$

Finally, combining the macroscopic results 2.18 and 2.20 and resubstituting the Chapman-Enskog expansions 2.15 one retrieves the Navier-Stokes of viscous compressible fluid flow. To complete the ‘‘Lattice Boltzmann’’ derivation the three transport coefficients of equation 2.1 are calculated. Sound speed and viscosities in model units are given by

$$\begin{aligned} c_s &= \sqrt{\frac{1}{\sigma}} \\ \eta &= \left(\tau - \frac{1}{2}\right) \sigma \sum_q t_q \varphi_q \\ \zeta &= \left(\tau - \frac{1}{2}\right) \left(2\sigma \sum_q t_q \varphi_q - \frac{1}{\sigma}\right) \quad . \end{aligned} \quad (2.21)$$

We now have the complete formulation of D -dimensional hydrodynamic ‘‘Lattice Boltzmann BGK Methods’’. The sound speed is tunable by altering the relative mass contents of different sub-lattices. The rest particles supply a buffer that ensures the local conservation laws. The shear viscosity may be varied by choosing appropriate relaxation times τ . Together, different Mach and Reynolds number ranges may be simulated.

For a numerical code a concrete lattice must be selected and the respective equilibrium distributions must be determined from above formulae. The choice is not as restricted as in the LGA case since there is no Fermi-like rule. For the sake of computational efficiency one tries to find the minimum necessary number of particle distributions. In three dimensions it is the ‘‘D3Q15’’ lattice geometry (Qian et al. 1992).

2.2.1 The D3Q15 Lattice

The “D3Q15” lattice consists of 15 nodes on three sub-lattices: (1) at $q=0$, the cell itself $(0,0,0)$ where the rest particles reside. (2) at $q=1$, the six nearest neighbors $(\pm 1, 0, 0)$, $(0, \pm 1, 0)$, $(0, 0, \pm 1)$ where the particles move with unit velocity. And (3) at $q=3$, the eight third-nearest neighbors $(\pm 1, \pm 1, \pm 1)$ where the packets move with a velocity of $\sqrt{3}$. This is the smallest possible number of nodes to fulfill all constraints for a 3D hydrodynamic model. Figure 2.2 shows a sketch of the “D3Q15” lattice geometry.

q	A_q	B_q	C_q	D_q
0	t_0	0	$-\frac{1}{3}$	0
1	$\frac{1-t_0}{7}$	$\frac{1}{3}$	$-\frac{1}{6}$	$\frac{1}{2}$
3	$\frac{1-t_0}{56}$	$\frac{1}{24}$	$-\frac{1}{48}$	$\frac{1}{16}$

Table 2.1: D3Q15 equilibrium coefficients to second order in velocity.

The “D3Q15” equilibrium coefficients are given in table 2.1. The respective transport coefficients read

$$\begin{aligned}
 c_s &= \sqrt{\frac{3}{7}(1-t_0)} \\
 \eta &= \frac{1}{3} \left(\tau - \frac{1}{2} \right) \\
 \zeta &= \left(\tau - \frac{1}{2} \right) \left(\frac{2}{3} - \frac{3}{7}(1-t_0) \right) .
 \end{aligned} \tag{2.22}$$

Thus is the definition of the basic 3D LBM BGK model that I have used in this thesis. The improvement of numerical stability, the necessary modifications for simulating dark cloud flows and the parallel code implementation for a cluster of workstations and for the CM-5 parallel supercomputer will be described in the next chapter.

The D3Q15 Lattice

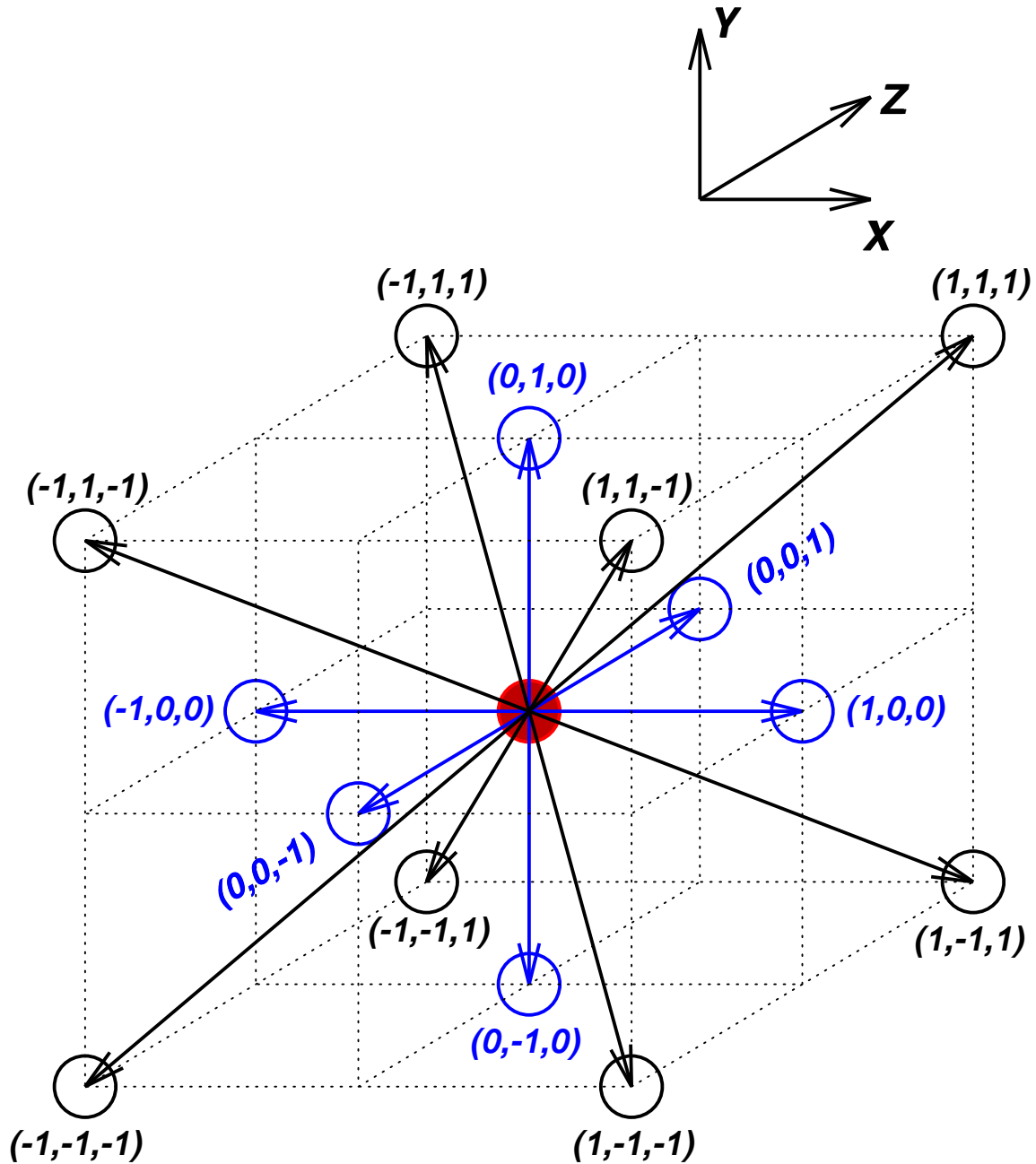


Figure 2.2: Sketch of the D3Q15 lattice geometry. The velocity directions of the 14 moving particle distributions are shown as arrows. In each time step the particle packets move along the predefined directions and then relax toward the Lattice-Maxwellian equilibrium distribution. The relaxation rate determines the physical viscosity.

Chapter 3

The Parallel Code

3.1 Numerical Stability

Since the “Lattice Boltzmann Method” uses a hybrid algorithm, which includes both integer and floating point operations, it potentially suffers from numerical instabilities. The stability of the “FHP” and “D3Q15” “Lattice Boltzmann” methods has been analyzed to some extent by Sterling and Chen (1996); it depends on the mass distribution among the discrete velocity directions, the mean flow velocity, the relaxation parameter ω and the wavenumber of perturbations. Mainly, it is necessary that $0 < \omega < 2$ so that the method is linearly stable. This also ensures that the viscosity is positive since $\eta_{D3Q15} = \frac{1}{3} \left(\frac{1}{\omega} - \frac{1}{2} \right)$. There is an absolute model velocity maximum above which the method is unstable. This maximum decreases for increasing ω . For the “D3Q15” lattice at $\omega = 2$ the maximum possible velocity is about $\frac{1}{3}$. It seems advisable that the model velocities be generally kept below this value.

Flow velocities in dark clouds are expected to be of the order on the sound speed since the spectral linewidths of the tracer molecules are at most a few times their respective thermal values. Therefore, to simulate Mach numbers of around unity, the model sound speed c_s should be tuned to a value lower than the maximum stable velocity of approximately $\frac{1}{3}$. To be on the safe side I have used $c_s = 0.1$ throughout the simulations. Nevertheless, my numerical tests have shown that the code becomes increasingly more unstable as the flow velocity approaches the sound speed. The problem seems to be the low order truncation in the Taylor’s series of the LBM derivation (equations 2.8 and 2.14). Chen et al. (1994) have derived higher order corrections for thermo-hydrodynamic LBMs. By fixing the thermal energy, these corrections may also be used for the purely hydrodynamic models. The new terms ensure the isotropy of all velocity tensors up to 6th order. The equilibrium distributions now are expanded to fourth order in velocity, i.e.

$$f_{qi}^{eq}(\rho, \vec{v}) = \rho \left(A_q + B_q(\vec{c}_{qi}\vec{v}) + C_q\vec{v}^2 + D_q(\vec{c}_{qi}\vec{v})^2 \right. \\ \left. + E_q(\vec{c}_{qi}\vec{v})\vec{v}^2 + F_q(\vec{c}_{qi}\vec{v})^3 + G_q(\vec{c}_{qi}\vec{v})^2\vec{v}^2 + H_q\vec{v}^4 + \dots \right) \quad (3.1)$$

When calculating the new coefficients there are some free parameters. Their optimum values have to be determined by numerical tests on stability. Most critically, I find that one parameter (X_3 in Chen’s notation (Chen et al. 1994)) must be set to zero to get a good model. My optimum coefficients are listed in Table 3.1. With the new equilibrium distributions the stability improves somewhat with higher Mach numbers. Additionally, the often observed

q	A_q	B_q	C_q	D_q	E_q	F_q	G_q	H_q
0	t_0	0	$-\frac{1}{3}$	0	0	0	0	0
1	$\frac{1-t_0}{7}$	$\frac{1}{3}$	$-\frac{1}{6}$	$\frac{1}{2}$	$-\frac{1}{2}$	$\frac{1}{2}$	0	0
3	$\frac{1-t_0}{56}$	$\frac{1}{24}$	$-\frac{1}{48}$	$\frac{1}{16}$	$-\frac{1}{16}$	$\frac{1}{16}$	0	0

Table 3.1: D3Q15 equilibrium coefficients to fourth order in velocity.

checkered patterns are reduced. These patterns are believed to be caused by the employed lattice structure.

Still present, however, are spurious instabilities due to the non-linear growth of large velocity gradients. In this case the current particle distributions f_{qi} are far away from their equilibrium values. These non-equilibrium distributions are, at first, localized to only a few cells but eventually spread through the whole data cube and lead to a global collapse. To prevent this growth I have developed a damping method which forces the current f_{qi} toward their respective equilibrium distributions by selectively lowering the relaxation parameter ω . This is equivalent to locally raising the viscosity. If a cell's velocity $|\vec{v}|$ exceeds a given limit v_0 , then the relaxation parameter for the next collision is changed according to

$$\tilde{\omega} = \omega_0 + (\omega - \omega_0) \frac{(\theta c_s)^2}{(|\vec{v}| + (\theta c_s - v_0))^2} \quad (3.2)$$

where θ defines the “sharpness” of the decrease. ω_0 is a lower limit which has been included since the BGK relaxation process produces increasingly more non-hydrodynamic modes if $\omega \ll 1$ (Behrend et al. 1993).

The above damping method drastically improves the stability so that flows at Mach numbers of up to around 0.9 can now be simulated. Simultaneously the behavior at low viscosities has improved so that simulations up to a Reynolds number of around $10^{4.5}$ are possible. Thus, the model is suited to simulate dark cloud flows. Reasonable values for θ lie between 0.01 to 0.1. ω_0 should be between 0.7 and 1.3 depending on the value of the global relaxation parameter ω . Yet, despite all improvements a global flow velocity at “Mach One” currently seems to be the absolute upper limit for the “D3Q15” model and other LBMs. At higher Mach numbers the velocity gradients which occur are too large and, thus, cannot be accounted for.

3.2 Miscible Fluid Formalism

Tracer molecules allow us to observe interstellar clouds since the hydrogen itself does not emit radiation at the low cloud temperatures of 10 – 100 K. However, due to varying excitation conditions or varying abundances the tracers are not necessarily homogeneously distributed. Therefore, the numerical model must include two miscible fluid phases, the hydrogen and the tracer molecules. The second phase has been realized by adding another set of 15 particle distributions to the original “D3Q15” method. To distinguish both phases I will call them “red” (f_{qi}^r) and “blue” (f_{qi}^b). Individual and total densities and velocities are defined by

$$\begin{aligned}
 \rho^r &= \sum_{qi} f_{qi}^r \\
 \rho^b &= \sum_{qi} f_{qi}^b \\
 \rho &= \sum_{qi} (f_{qi}^r + f_{qi}^b) \\
 \vec{v}^r &= \frac{1}{\rho^r} \sum_{qi} f_{qi}^r \vec{c}_{qi} \\
 \vec{v}^b &= \frac{1}{\rho^b} \sum_{qi} f_{qi}^b \vec{c}_{qi} \\
 \vec{v} &= \frac{1}{\rho} \sum_{qi} (f_{qi}^r + f_{qi}^b) \vec{c}_{qi} .
 \end{aligned} \tag{3.3}$$

The fluid mixing is done via calculating new distribution functions $\widetilde{f}_{qi}^{r/b}$ before the particles collide. Miscibility requires only global momentum conservation. The momentum information for the individual components is lost. Mass conservation must be ensured for both fluids separately. The intermediate particle packets are therefore

$$\begin{aligned}
 \widetilde{f}_{qi}^r &= \frac{\rho^r}{\rho} (f_{qi}^r + f_{qi}^b) \\
 \widetilde{f}_{qi}^b &= \frac{\rho^b}{\rho} (f_{qi}^r + f_{qi}^b) .
 \end{aligned} \tag{3.4}$$

The relaxation process is governed by one global Boltzmann equation where the “red” and “blue” parts follow according to the individual mass contents

$$\begin{aligned}
 \widetilde{f}_{qi}^r(\vec{r} + \vec{c}_{qi}, t + 1) &= \widetilde{f}_{qi}^r(\vec{r}, t) - \frac{1}{\tau} \left(\widetilde{f}_{qi}^r(\vec{r}, t) - f_{qi}^{eq}(\rho^r, \vec{v}) \right) \\
 \widetilde{f}_{qi}^b(\vec{r} + \vec{c}_{qi}, t + 1) &= \widetilde{f}_{qi}^b(\vec{r}, t) - \frac{1}{\tau} \left(\widetilde{f}_{qi}^b(\vec{r}, t) - f_{qi}^{eq}(\rho^b, \vec{v}) \right) .
 \end{aligned} \tag{3.5}$$

To test the two-phase formalism I have simulated the three-dimensional diffusion of an initial single dot of tracer fluid into a homogeneous background medium. The analytical solution predicts a Gaussian tracer distribution which evolves in time according to

$$\rho_{tracer} \sim t^{-\frac{3}{2}} e^{-\frac{1}{4}r^2 \bar{D}^{-1} t^{-1}} \tag{3.6}$$

where r is the radial distance from the initial dot position and \bar{D} is the diffusion coefficient. Figure 3.1 shows the numerical results for $\omega = 1.99$ at three different time steps. For t_0 a Gaussian fit to the data has been made. The curves for $2t_0$ and $4t_0$ have been calculated from equation 3.6. They show that the data follows the theory reasonably well. Remaining deviations are due to the lattice discretization and rounding errors.

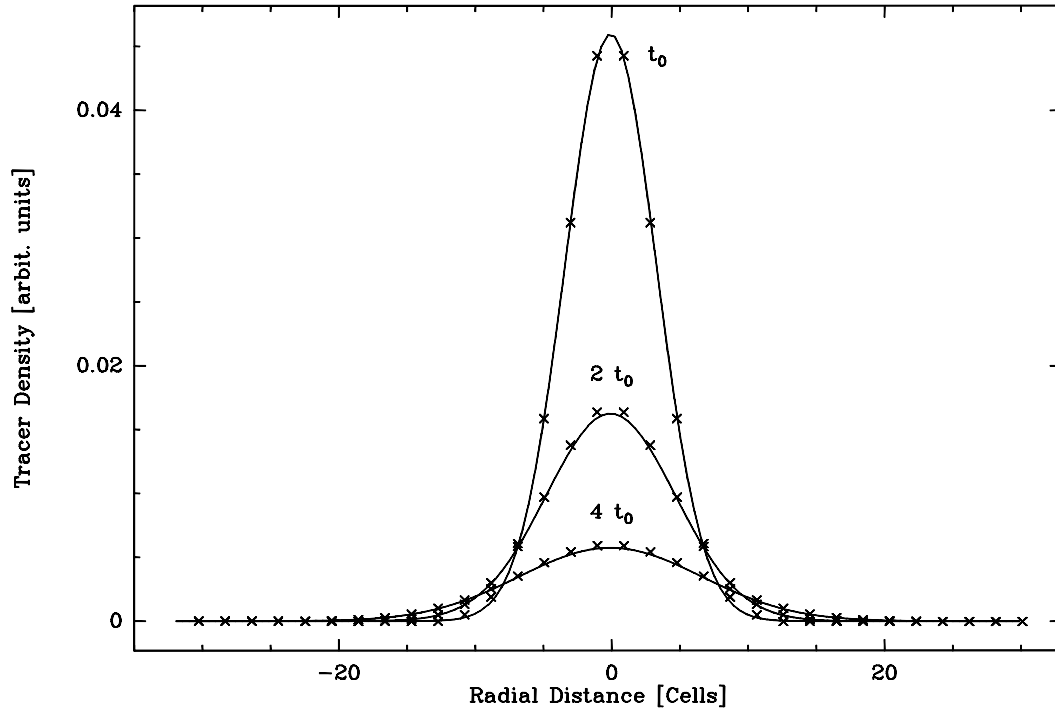


Figure 3.1: The two-phase formalism has been tested by simulating the diffusion of an initial single dot of tracer fluid into a homogeneous background medium at $\omega=1.99$. The analytical solution to this problem predicts a spatial Gaussian tracer distribution evolving in time. The crosses mark the measured density profiles at three different time steps. A Gaussian fit has been made at t_0 . The curves for $2t_0$ and $4t_0$ have been calculated from the analytical formula. They fit the data reasonably well.

3.3 Initial and Boundary Conditions

Initial conditions are usually specified in terms of densities and velocities. For the “Lattice Boltzmann Method” these macroscopic values have to be translated into corresponding microscopic particle packets for each fluid phase. A common way, which has been followed in this study, is to use the respective equilibrium distributions (equation 3.2) for this translation.

First, in my code a background field is established for the whole data cube. Later, during the simulation, matter may flow into or out of the cube through square or circular inlets or outlets of arbitrary size and spatial position. These sources and drains may be oriented parallel to any of the cube surfaces. The surfaces themselves can also be continuously set to initially defined values of density and velocity to allow the implementation of various boundary conditions. The nominal values of ρ and \vec{v} at the inlets may be varied randomly to induce flow instabilities. I have not included any periodic forces since they would imprint a systematic pattern onto the flow.

Without any special settings the boundary conditions are periodic along all three axes because the free streaming of particles has been realized via circular shifts of the three-dimensional arrays. These shift operations are provided in the standard command set of the parallel programming languages that I have used (see section 3.4). Circular shift up by one, for example, applied to a 1D vector A containing N elements, means that $\widetilde{A}(2) = A(1)$, $\widetilde{A}(3) = A(2)$,

..., $\widetilde{A}(N) = A(N - 1)$ and $\widetilde{A}(1) = A(N)$.

The previously mentioned marker array is used to store 3D “objects” of arbitrary shape. A number of special cell conditions have been implemented. A cell may be reflective, i.e. part of a solid body like a wall. In this case the incoming particle packets are bounced back by 180° . This ensures that the time averaged velocity at the wall vanishes and that there is a dragging force between fluid and wall. No relaxation should take place in the reflective cells since ρ and \vec{v} are not always properly defined due to possible missing particle packets on the inside of an object.

Next, a partly permeable cell has been defined. Part of the kinetic energy may be absorbed by the cell so that the flow is decelerated. This allows for the simulation of scenarios where tracer molecules are thermally evaporated off the dust grains or where cold dense clumps move through a background medium while parts of the clumps are torn off by viscous forces. Letting the “red” fluid phase be the background gas and the “blue” phase represent the tracer molecules the energy absorption and tracer molecule release can be calculated microscopically via

$$\begin{aligned}
 f_{00,final}^r &= \rho^r - \sqrt{1 - \frac{2e_{rel}}{\rho\vec{v}^2}} (\rho^r - f_{00,initial}^r) \\
 f_{qi,final}^r &= \sqrt{1 - \frac{2e_{rel}}{\rho\vec{v}^2}} f_{qi,initial}^r \quad \forall q \neq 0 \\
 f_{00,final}^b &= \rho^b - \sqrt{1 - \frac{2e_{rel}}{\rho\vec{v}^2}} (\rho^b - f_{00,initial}^b) + \rho_{rel}^b \\
 f_{qi,final}^b &= \sqrt{1 - \frac{2e_{rel}}{\rho\vec{v}^2}} f_{qi,initial}^b \quad \forall q \neq 0
 \end{aligned} \tag{3.7}$$

where e_{rel} is the absorbed specific energy and ρ_{rel}^b is the amount of material released into the gas phase.

A similar algorithm has been used for special absorber cells. During the first simulation runs it happened that tracer gas passed the cube boundaries via the periodic conditions and reentered the cube at the inlet. This caused the superposition of two unrelated patterns. Therefore, I have employed a one-layer filter at the cube’s end to absorb one of the two fluid phases. In this case the velocity as well as the density are multiplied by a given factor which was typically around 0.01. It is not possible simply to set $\rho^b = 0$ and $\vec{v}^b = \vec{0}$ since this causes numerical instabilities.

The introduced cell types may occur at arbitrary positions in the cube since all cell related calculations are purely local. In my program I have included some basic geometric elements like square and circular plates, cylinders and arbitrarily oriented general ellipsoids. These can be used to construct more complex setups. The possibility to implement complex geometries is one of the major advantages of LBMs over other CFD methods.

3.4 Parallelization

For investigations in the structure of 3D hydrodynamics a minimum cube size of around 100^3 cells is necessary. With the two-phase BGK code it would take ~ 50 hours and around 120 MByte of main memory to calculate a couple of thousand timesteps on a typical workstation. This is far too high to make a systematic examination of different setups. Therefore, the distribution of the work load among several computers is needed. The BGK method is an ideal candidate for parallel execution since most of the calculations are done locally. Only the free streaming of particles along the lattice links requires communication between the processors. If the data layout is chosen appropriately the communication time can be minimized.

3.4.1 Message Passing Paradigm

The basic idea behind parallelization is to distribute a global problem among a number of separate processors. Under the “Multiple Instruction Multiple Data” (MIMD) concept each computing node calculates independently intermediate local results. Inquiry messages are sent over an interconnecting network whenever a partial result is needed by another node (“Message Passing”). The sending node must wait until the appropriate data is available before it can resume its work. To avoid idle times it should be ensured that the workload is distributed evenly according to the individual node computing powers.

Quite a number of subroutine libraries have been developed to allow sending and receiving messages. The “Parallel Virtual Machine” (PVM⁷, Beguelin et al. (1991)) has become a rather popular system since it supports heterogeneous clusters of workstations, a computing resource which is already available at many institutes, but rarely used. Under PVM a special program (a daemon) is started on each of the nodes. Messages are sent to the daemon, passed on to the recipient computer’s daemon and eventually to the node program.

Currently there is an attempt of an international group of computer users and vendors to specify a standardized set of message passing routines based on PVM and other libraries. The new standard is called “Message Passing Interface” (MPI⁸) and its main goal is to help writing portable software.

3.4.2 Data Parallel Paradigm

The “Message Passing” concept allows for the handling of all kinds of problems, especially if different subproblems with different sets of data are to be solved asynchronously. However, one would often just like to increase data space and performance of a synchronous algorithm working on a homogeneous dataset. The respective parallelization concept is called “Single Instruction Multiple Data” (SIMD) or “Data Parallel” paradigm. The same program is executed by all processors in parallel but each of them works on its individual piece of data. The SIMD concept is especially suited for problems like the hydrodynamics simulations presented in this thesis. The data space of the three-dimensional models grows rapidly as the linear resolution is raised but the algorithm always stays the same.

Some of the current massively parallel architectures are specialized for support of the data parallel paradigm. Special programming languages have been developed to facilitate the porting of existing serial programs. The “Connection Machine 5” (CM-5, TMC (1993), see Figure 3.2) is one of these systems (actually the CM-5 supports both the MIMD *and* the SIMD paradigm). The CM-5 consists of control processors (CPs) which supervise partitions of computing nodes. The nodes in turn may be equipped with vector units so that a combined parallel vector architecture results. A CM-5 program is started on one of the CPs. This is called the “host” program. In turn the host starts up the jobs on the node processors. Parallel data resides in the nodes’ memories while scalar variables are stored in the host program. Furthermore, the host executes all scalar operations including scalar loops. Whenever a parallel command is to be executed, the host sends it directly to the network of nodes and waits for its completion.

⁷WWW-URL: <http://www.epm.ornl.gov/pvm>

⁸WWW-URL: <http://www.mcs.anl.gov/Projects/mpi/index.html>

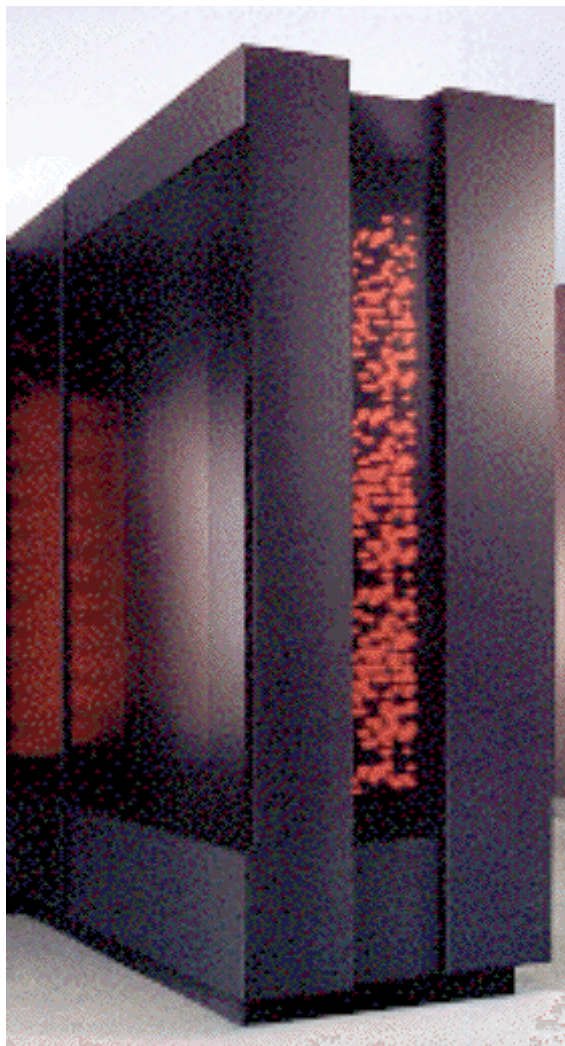


Figure 3.2: The CM-5 parallel supercomputer used for part of the 3D hydrodynamical simulations. A 64 node CM-5 has been installed at the “Gesellschaft für Mathematik und Datenverarbeitung” (GMD, WWW-URL: <http://www.gmd.de>) in St. Augustin in September 1993. Each of the processing nodes has 4 vector units giving a total peak performance of 8 GFLOP. (Image Courtesy Thinking Machine Corporation, WWW-URL: <http://www.think.com>)

On the CM-5 a special version of FORTRAN called “Connection Machine FORTRAN” (CMF) is available. It allows direct arithmetic operations on parallel multidimensional arrays, conditional programming dependent on parallel arrays, parallel loops etc. One special command (CSHIFT) allows the parallel circular shifting of array elements which is needed for the free streaming step in the “Lattice Boltzmann Method”. In fact, this is the only command in the LBM that needs internode communication since elements may be shifted across node memory boundaries toward neighboring nodes.

CMF is a special product of one vendor (TMC). To standardize data parallel programming there is an initiative similar to the definition of MPI. The new parallel programming language standard is called “High Performance FORTRAN” (HPF, Koelbel et al. (1994)). HPF structures are similar to CMF.

3.4.3 ADAPTOR

A group at the GMD⁹ in St. Augustin near Bonn has developed a source to source transformation package called “Automatic DATA Parallelism TranslatOR” (ADAPTOR¹⁰, Brandes (1993)) to make the data parallel paradigm available for explicit message passing systems like PVM. ADAPTOR accepts FORTRAN 77 and important parts of FORTRAN 90, CMF and HPF as input and produces parallel code for a number of different communication models (PVM, MPI, CMMD, P4 etc.).

ADAPTOR supplies the original program structure with the necessary message passing subroutines to distribute the data among an arbitrary number of computing nodes. New FORTRAN programs are created which must then be compiled and linked with the message passing library. The output programming language for these new programs may be selected according to available compilers (F77, F90, F95, Vector FORTRAN etc.).

Again, the parallel arrays are stored in the node programs. Scalar variables, however, are not only stored in a host program but they are replicated on each node job. Thus, there is no need for continuous communication to fetch scalar variables. Only if data is read or written from or to files does the host broadcast the new values to all nodes. Essentially this is a mixed MIMD and SIMD model since all node processes work independently once they have retrieved all necessary scalar variables.

With ADAPTOR, parallel programming becomes readily feasible even for workstations equipped with a normal F77 compiler and PVM only. Therefore, it provides a very powerful and easy to use development tool.

3.5 Code Implementation

The “Lattice Boltzmann” algorithm has been implemented by using the FORTRAN and C programming languages. The flowchart diagram in Figure 3.3 shows the general program structure. Each individual particle distribution and the marker field is stored in a separate three-dimensional array. The program first reads a parameter file which specifies the data cube size, the relaxation parameter, the model sound speed, the number of time steps, the boundary conditions and the necessary geometries. Next, the geometries are written to the marker field.

⁹Gesellschaft für Mathematik und Datenverarbeitung mbH / Forschungszentrum Informationstechnik GmbH; The German National Research Centre for Mathematics and Computer Science / German National Research Center for Information Technology; WWW-URL: <http://www.gmd.de>

¹⁰WWW-URL: <ftp://www.gmd.de/gmd/adaptor>

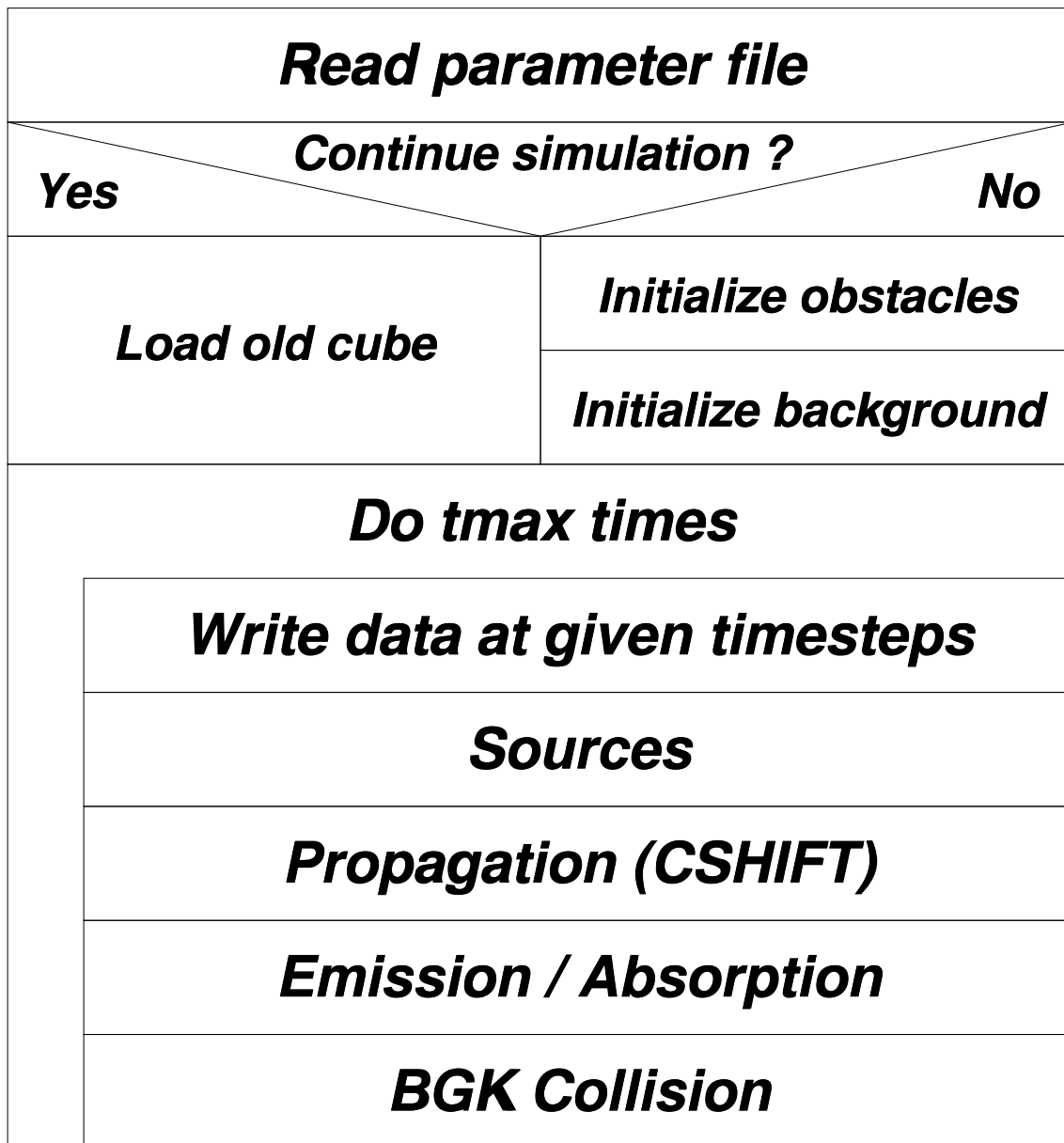


Figure 3.3: General program structure of the “Parallel 3D Lattice Boltzmann Code”. The parameter file, which is read first, contains information about data cube size, relaxation parameter, model sound speed, geometries etc. The geometries are written to a special marker array (“Initialize obstacles”). The background density and velocity are translated into the respective equilibrium particle distributions (“Initialize background”). The time loop consists of four major blocks. First, the possible sources are set. Next, the particles are propagated along their assigned lattice directions into the neighboring cells. Then, possible emission and absorption effects are handled. Finally, the particles collide using the BGK relaxation method. Note that in the parallel code only the propagation step (“CSHIFT”) needs node to node communication. Any other operation is fully local. This makes the method extremely efficient on parallel architectures.

The background density and velocity are translated into the respective equilibrium particle distributions. The time loop consists of four major steps. First, possible sources are applied by again using the $(\rho, \vec{v}) \rightarrow f_{qi}^{eq}$ translation. Then the particles' free streaming is accomplished via circular shift operations. Next, emission and absorption cells are handled. Finally, the "red" and "blue" particles are mixed and their collision is calculated using the BGK relaxation method.

After developing and testing the single computer version, I carried out the parallelization. First, I used PVM and ADAPTOR to get a code for the cluster of workstations at the MPIfR. Later, I was granted computing time on the 64 node parallel supercomputer CM-5 located at the GMD. For the CM-5 the PVM/ADAPTOR code had to be substantially modified to optimally exploit the parallel vector architecture.

3.5.1 PVM/ADAPTOR Solution

To parallelize the "Lattice Boltzmann Method" under PVM and ADAPTOR I have used a "host+node" model. One program (the host) is started on one computer. The host starts node processes on all networked computers and it handles all input/output operations. After reading variables they are directly passed on to the nodes so that continuous host-node communication is not necessary.

To be able to change the data cube size without recompilation, all three-dimensional arrays have been made allocatable, i.e. their size is set only at run time. This alternative also proved to be faster than using fixed array sizes. The arrays have to be distributed somehow among the available nodes. One must choose whether to distribute an axis onto the nodes or whether to keep it completely local. The number of distributed axes should be kept low since distribution implies the possible need for communication. Node to node communication over the network is always slower than direct local access to variables.

The slowest varying axis should be distributed first in order to optimize the local computations under PVM/ADAPTOR. Complying with the FORTRAN standard I kept the first two indices local and distributed only the third one. Numerical tests with the alternative layouts showed that they were up to 4 times slower. The data layout may be defined by special CMF or HPF directives. The necessary CMF version reads `CMF$LAYOUT <ArrayName>(:SERIAL, :SERIAL, :NEWS)`. Its HPF counterpart is `!HPF$DISTRIBUTE(*, *, BLOCK) :: <ArrayName>`. "SERIAL" or "*" stands for a local axis while "NEWS" or "BLOCK" stands for a distributed axis. The data will always be evenly distributed among the available nodes. An outline of the employed data layout is shown in Figure 3.4. For all explicit loops over the local inner two indices I additionally issued the `!HPF$INDEPENDENT, LOCAL_ACCESS` directive which indicates that no parallel operations occur in those loops. This helps ADAPTOR to produce optimized local code.

At the time of developing the parallel LBM code neither ADAPTOR nor PVM were able to support parallel input/output operations. Thus, the calculated data cubes had to be transferred to the host to be written as a file. ADAPTOR supplies a special "host" variable type which has only one incarnation in the host process. Only these variables may be used for input/output. Since the three-dimensional arrays are sometimes rather large, it is advisable to transfer and write the data slicewise. This saves host program memory which can be used for larger data cubes. A loop over the distributed third axis gradually copies two-dimensional planes into the host's memory and appends them to the output file. The array input/output routines have been written using the programming language C since there is much less memory overhead than in FORTRAN.

Data distribution under PVM

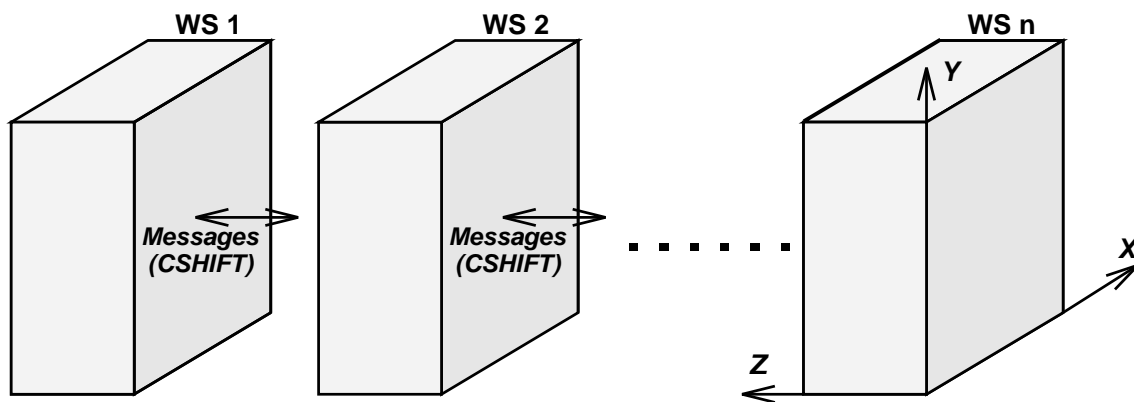


Figure 3.4: The data distribution under PVM on the cluster of workstations. This layout has been used for all three-dimensional arrays, i.e. the 2×15 particle distributions and the cell marker array. The third axis (Z) has been distributed since it is varying the slowest in the FORTRAN environment. This ensures that the local loops can be fully optimized by the compiler.

Recently a “Parallel Input/Output System” (PIOUS¹¹, Moyer and Sunderam (1995)) for PVM has been introduced. This package allows for the writing of data directly from the node processes onto the disks connected to the nodes. The network transfer of huge amounts of data is thus circumvented. PIOUS will be used in a future version of the LBM code.

Normally, the complete set of particle distributions is written to a file to be able to continue the simulation later. However, the data cubes may be rather large (several hundred megabytes) so that online data reduction is necessary, especially if a time evolution is to be saved to disk. I have therefore added a subroutine which calculates the actual density and velocity fields and discretizes them down to 8 bits. The loss of accuracy is bearable for visualization and animations. However, to calculate individual maps and spectra the full floating point data have been used.

The code produced by ADAPTOR can be used with an arbitrary number of nodes. Thus, the LBM program can run on any cluster of workstations. So far, I have successfully tested the code on a heterogeneous cluster consisting of HP-UX, SunOS and Solaris workstations at the MPIfR.

3.5.2 CMF Solution

The situation on the CM-5 is quite different compared to the PVM/ADAPTOR model. “Connection Machine FORTRAN” (CMF) is optimized for using fixed size fully distributed parallel arrays, i.e. (:NEWS, :NEWS, :NEWS) layout works best. Parallel operations should always work on the whole three-dimensional arrays. However, this implies the generation of a number of temporary three-dimensional arrays.

The `WHERE` command is one of the parallel statements which may need additional temporary memory. `WHERE` is the parallel equivalent of the serial `IF` command. A typical line in CMF code might be `WHERE(A.GT.0) B=SQRT(A)` where `A` and `B` are parallel arrays. To execute this

¹¹WWW-URL: <http://www.mathcs.emory.edu/pious.html>

command, first, a logical condition mask is calculated. In this example the array would hold the values of the expression $(A.GT.0)$. Next, array B would be set according to the values in the temporary array. The mask is as big as the involved arrays so that rather large amounts of memory may be allocated in the case of higher-dimensional variables. More temporary fields are necessary if the logical expressions are more complicated. Thus, the memory available for the data cube is drastically reduced.

The problem is far less severe if the temporary arrays are only two-dimensional. This may be reached if the cube is sliced into planes. A serial loop on the host indicates the plane number. This loop should run over a local axis. Due to internal data representation the optimal layout for three-dimensional arrays is now $(:SERIAL, :NEWS, :NEWS)$. The scalar loop thus runs over the first index. Using this method it is possible to exploit the CM-5 parallel vector architecture and to minimize the additional temporary storage needs.

All remaining two-dimensional explicit loops had to be transformed into CMF specific commands. Mostly, the `FORALL` statement had to be used. It is flexible enough to set the necessary geometries in one step. To set a circular disk in a two-dimensional array A at offset (J_0, K_0) with radius R one would, for example, use `FORALL(J=1:JMAX, K=1:KMAX, (J-J0)**2+(K-K0)**2.LE.R**2) A=1.`

Finally, input/output on the CM-5 is simpler than using PVM because the Connection Machine is equipped with a parallel scalable disk array (SDA) which allows the nodes to directly write to a distributed hard disk system. Compared to PVM/ADAPTOR this is very fast and easy to use. In FORTRAN a simple `WRITE` command is sufficient.

3.6 Code Performance

The performance of parallelized programs is to some degree dependent on the implementation details. The direct comparison of both codes is difficult because major changes were necessary for the CM-5 version. Performance also depends on problem size and geometry.

The PVM/ADAPTOR code has been used mainly on three HP 735⁺ workstations with roughly 50 MFLOP peak performance each. All three are equipped with at least 144 MByte main memory. Given the fact that there is a certain limit above which swapping starts and that one machine has to be used for input/output and thus needs additional storage, the total memory for 3D data is at most 330 MByte. Thus, the maximum problem size on the three workstations was around 140^3 cells. The individual workstations in the network should have comparable performances since the data is evenly distributed among the nodes. Slow or heavily used workstations decrease the total code performance.

If the datacube is rather small (e.g. 32^3 volume elements), then most of the time is spent for sending and receiving the messages. The load on each of the three machines never rises above ~ 20 to 30% CPU time so that there is no real time gain. It might even take longer than on a single computer to complete the job. The ratio of the time needed for message passing versus the time spent for local calculations decreases for larger cubes since the total number of cells grows faster than the number of cells to be passed between the nodes.

The peak performance on three HP 735⁺ workstations for the two-phase code, without emission and absorption, i.e. measuring the pure "Lattice BGK" procedure, lies around 230,000 cells per second excluding input/output. The mean performance for a typical dark cloud flow setup including an ample amount of emitting and absorbing cells is roughly 112,000 cells per second. Calculating, for example, 6000 time steps of the evolution of a $270 \times 90 \times 90$ cube thus takes 33 hours CPU time.

The CMF code has been used on the 64 node CM-5 of the GMD. Each of the nodes exhibits a performance of 128 MFLOP including the vector units. Together the maximum peak performance is 8 GFLOP. Each node has 32 MByte main memory adding up to a total of 2 GByte. Some memory is needed by the system and the program text. Thus, the maximum problem size is roughly 250^3 cells. A scalable disk array (SDA) of more than 20 GByte is connected to the CM-5. It may be used for parallel input/output directly from the nodes at a rate of 20 MByte per second. At the GMD the CM-5 is partitioned into 16+16+32 nodes during daytime and to the full 64 nodes during weekends and public holidays.

The CMF code performance is partly determined by the time needed for the scalar loop over the serial axis. This cube axis should therefore be the shortest. All axis lengths should be multiples of 8 to fully exploit the vector units (VU). The larger the absolute sizes the more efficiently the VUs are used since the computational overhead decreases. Taking again the typical dark cloud setup the performance for the two-phase code on 64 CM-5 vector nodes is about 1,400,000 cells per second for a cube size of $64 \times 64 \times 256$ cells. It increases to roughly 1,800,000 cells per second for a data cube size of $96 \times 96 \times 384$ cells. The peak performance for a large two-phase flow without special cells is 2,500,000 cells per second.

3.7 Simulation Examples

To show the capabilities of the code, I have done several test simulations. In the first example (Figure 3.5) a localized circular stream flows at a Mach number of 0.8 into a homogeneous background medium that is first at rest. The inlet density and velocity has been perturbed randomly to induce the shear instability. No periodic forces have been applied in order to avoid systematic initial patterns. The second fluid phase has been used to trace the jet streamlines. The image shows a volume rendering of the second fluid's density. The flow hits a hard sphere centrally. At the sphere's surface the velocity component perpendicular to the surface must vanish. The resulting shear forces create vortices which eventually become turbulent. Based on the sphere's diameter as typical length scale, the Reynolds number is $Re = 800$. This value is close to the classical critical Reynolds number of $Re_{cr} = 2000$. Thus, we observe in this example the transition between laminar and turbulent flow.

The second example shows the time development of an unsteady wake behind a cylinder (Figure 3.6). The fluid flows from left to right with a Mach number of 0.3. The cylinder is elongated perpendicular to the inflow. Through three small inlets on the left wall the second fluid is continuously injected in order to trace the stream structure. The image shows the tracer's integrated density. Based on the cylinder's diameter the range of critical Reynolds numbers for this type of problem lies between 160 and 210. I have used $Re = 300$ which is well above the upper limit. Yet, for much higher Reynolds numbers ($> 10^3$) the alternating wake structure declines and an isotropically turbulent tail develops behind the cylinder.

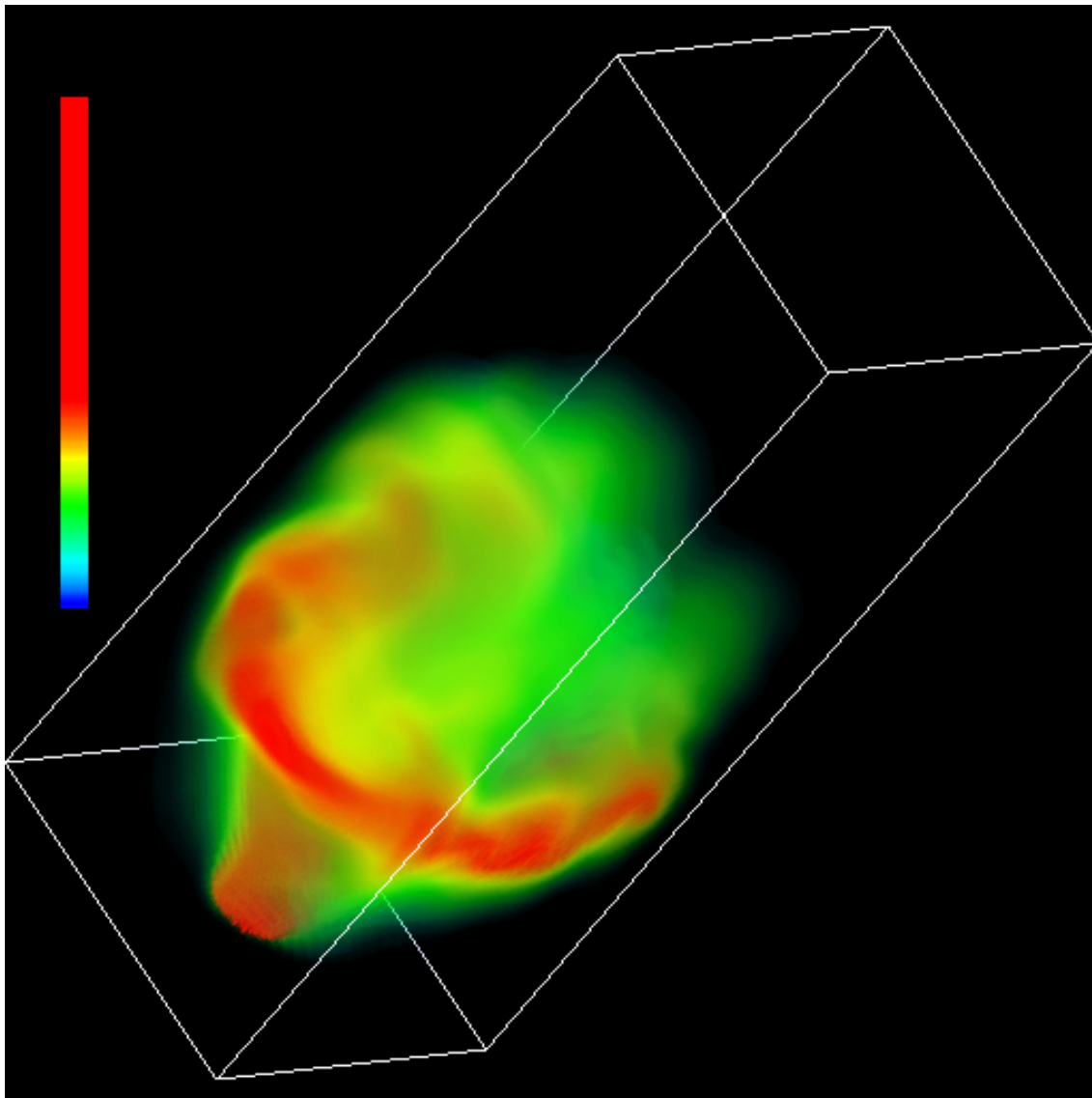


Figure 3.5: Turbulent flow around a hard sphere. One fluid phase of the “Lattice BGK” code has been used to model a stream of matter that flows at a Mach number of 0.8 into a homogeneous background medium which initially is at rest. The image shows the density of the second fluid phase which has been used to trace the main flow. The flow hits a hard sphere centrally. Based on the sphere’s diameter the Reynolds number is 800. Shear forces generate vortices which indicate developing turbulence. The wedge shows the tracer density color coding. (Volume rendering visualization done with AVS (WWW-URL: <http://www.avs.org>)).

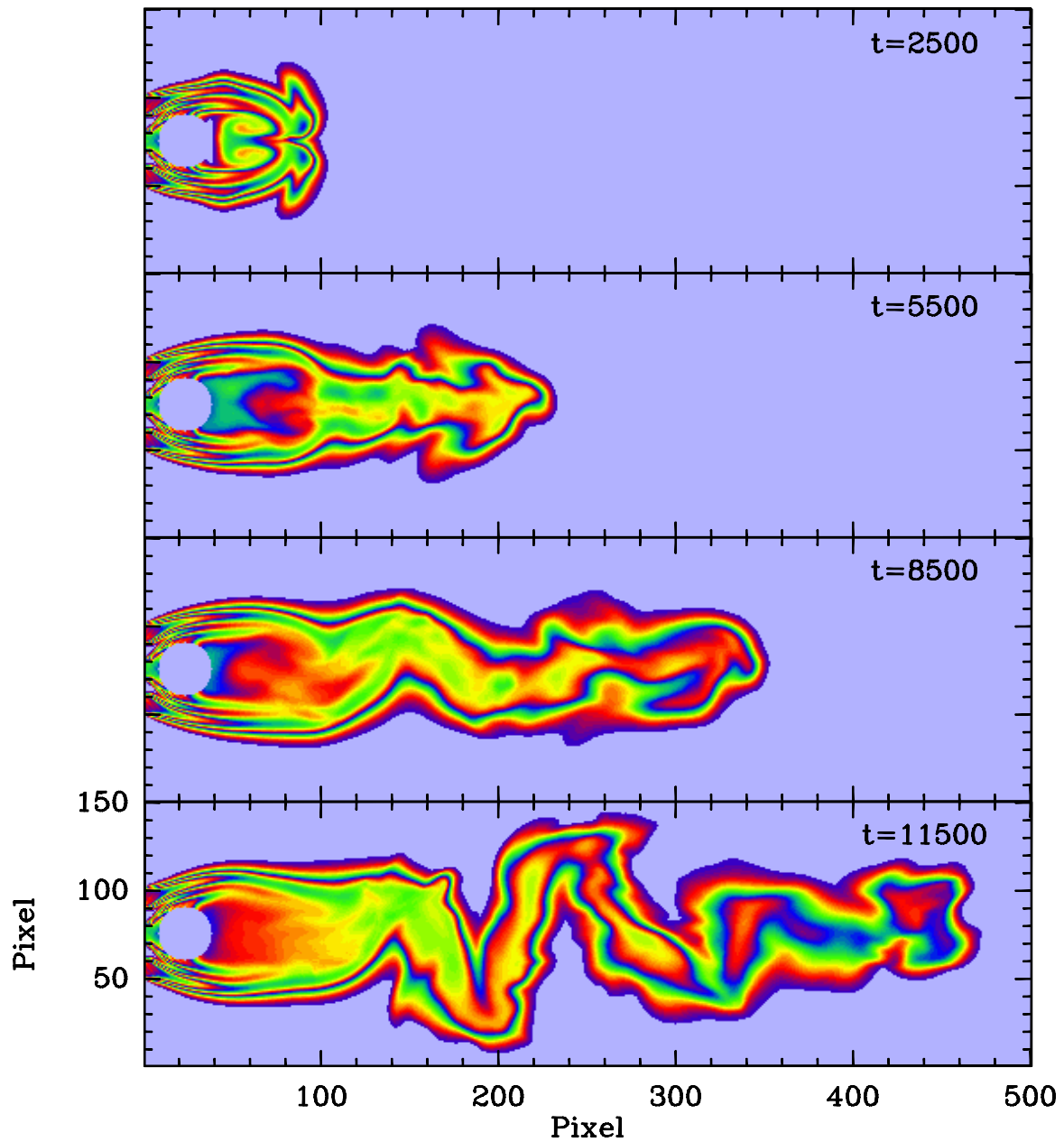


Figure 3.6: This example shows a time sequence of 2D projections of the development of a wake behind a cylinder. The fluid flows from left to right with a Mach number of 0.3 and a Reynolds number of 300 taking the cylinder's diameter as typical length scale. Space and time coordinates are given in model units. The depth of the cube along the cylinder was 20 pixels. The second fluid phase has been used to trace the development of the streamlines. It acts like smoke in a wind tunnel. At three different spots on the left border the tracer fluid is injected continuously. Its integrated density is coded by the colors in this image. To induce the instability in the otherwise fully symmetric geometry, I have perturbed the incoming fluid. Note that these variations have been applied randomly as opposed to the often used periodic forces.

Chapter 4

Simulations

The parallel 3D “Lattice Boltzmann Codes” have been used to numerically explore turbulent flows and their contribution to the spatial and velocity structure of interstellar dark clouds. Quiescent dark clouds are free of the “disturbing” physical processes accompanying massive star formation. Therefore, only mechanical energy input has been considered. My present simulations consist of collimated flows into a homogeneous background medium and the motion of dense clumps through an ambient medium. In the latter case I allow parts of the clumps to be torn off, so that a turbulent tail develops. No initial hierarchical clumpy or filamentary structure is presumed. Therefore, all emanating patterns result from the hydrodynamic evolution.

For all geometries the dependence of spatial and velocity structure on Reynolds and Mach numbers has been studied. The hydrodynamic Reynolds number is defined by

$$Re = \frac{Lv}{\nu} \quad (4.1)$$

where L and v are typical length and velocity scales and ν is the kinematic viscosity (Reynolds 1883). According to Lang (1980) the Reynolds number for neutral hydrogen gas is given by

$$Re = 2 \cdot 10^4 \rho L v T^{-\frac{1}{2}} \quad (4.2)$$

where ρ is the gas density and T is the kinetic temperature. Thus, the average dark cloud hydrodynamic Reynolds number is of the order 10^6 to 10^7 . The present simulations cover a range of Reynolds numbers from as low as a few hundred up to around $Re = 10^{4.5}$. The upper limit is given by the spatial flow resolution and by numerical instabilities which develop above the limit. However, I will show that the typical dark cloud structure is seen at intermediate Reynolds numbers below $10^{4.5}$.

From observational data one can also estimate a range of suitable Mach numbers

$$Ma = \frac{v}{c_s} \quad (4.3)$$

where c_s is the sound speed. The kinetic temperatures of quiescent clouds are low (10 – 100 K) and the observed molecular linewidths are at most a few times their respective thermal value $\Delta v_{thermal}$. This implies that the flow velocities are of the order of the local sound speed since

$$\Delta v_{thermal} = \sqrt{8 \ln(2) \frac{kT}{M}} = \sqrt{8 \ln(2) \frac{k\mu_{H_2}}{\gamma RM} c_{s,H_2}} \quad (4.4)$$

where k is Boltzmann's constant, R is the gas constant, μ_{H_2} is the hydrogen molecular weight, M is the mass of the tracer molecule and γ is the ratio of specific heats ($\frac{7}{5}$ for diatomic molecules). The tracer molecules are much heavier than the dynamically relevant hydrogen so that $\Delta v_{thermal}$ is only a small fraction of c_{s,H_2} . Thus, non-gaussian spectra may result even from *subsonic* flows. In the subsequent simulations a range of Mach numbers from 0.3 to 0.9 will be explored.

The comparison with observations requires the calculation of projected maps and spectra. Presently, I assume optically thin radiation so that the intensity is proportional to the integrated density along the line of sight. I will always show normalized column densities, since the models are, a priori, scale-free. The velocity information is used to derive artificial spectra. Hydrodynamical simulations normally cannot reproduce the observed smooth spectra since they average over a huge number of atoms or molecules and condense all microscopic statistical information into just one parameter which is the local temperature. Thus, each computational cell provides one sharp line. This also applies for the "Lattice Boltzmann Method" since it works on particle packets instead of single molecules. Spectral observations, on the other hand, reveal the thermal motion of the molecules via broadened lines. It is therefore necessary to convolve the simulated sharp spectra with a Gaussian having thermal linewidth as defined in equation 4.4. The linewidth depends on the tracer molecule's mass. Here, I will show spectra for the case of sulphur monoxide since this molecule will later be used for the comparison with observations (see chapter 5). All spectral maps will be oriented at a viewing angle of 45° relative to the main flow axis. This is a mean projection angle which avoids the rather improbable cases of a parallel or perpendicular view.

4.1 Collimated Shear Flow

To study the structuring effects of viscous shear forces, I have calculated the evolution of a collimated flow into a homogeneous background medium at different Reynolds and Mach numbers. The flow has a circular inlet shape; ambient and inflowing gas have equal densities. Periodic boundary conditions are assumed along the two axes perpendicular to the inflow direction. The surface opposite to the inlet is a hard wall which prevents inlet gas from flowing backwards into the cube. The background gas is free of tracers while the inflowing matter contains a tracer. The tracer's density is 10^5 times lower than that of the main gas. Thus, it is dynamically irrelevant and just follows the path of the inflowing gas. Astronomically this type of flow may occur, for example, at the very ends of bipolar outflows when the gas has been slowed down to subsonic velocities. Viscous forces become increasingly important and lead to shear instabilities as the flow protrudes further into the quiescent ambient medium.

For the simulations it is necessary to slightly perturb the incoming flow in order to induce the instabilities. Otherwise the symmetric geometrical setup would lead to completely symmetric flows. To avoid imprinting systematic flow patterns, *no periodic* forces have been used. Only *random* variations of the inflow density and velocity of up to $\pm 10\%$ of the nominal values have been applied. The variations have been done continuously for each time step and across the inlet's surface so that their spatial and time scales are of the order of the unit lattice length and unit time. Thus, no large scale structures are introduced.

The flow's Reynolds number has been calculated by using the inlet diameter as typical length scale. Different Reynolds numbers have been simulated by varying the gas viscosity through the BGK relaxation parameter ω (see chapter 2). At low Reynolds numbers ($Re < 400$) the shear flow is laminar and symmetric (see Figure 4.1). Only one vortex develops at the tip of the flow when the moving gas enters the background medium. The viscosity is so large that any perturbation is completely damped. The spectra are thermal with only slight broadening at the boundary between background and inflow.

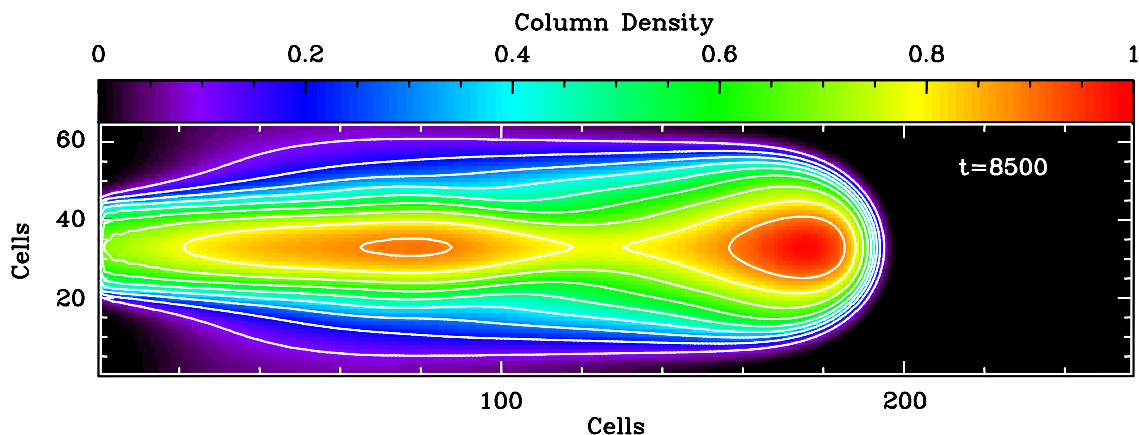


Figure 4.1: Collimated shear flow with a Reynolds number of 200 and a Mach number of 0.6. The plot shows the integrated intensity perpendicular to the main flow direction after 8500 timesteps. The length of the third axis was 64 cells. At these low Reynolds numbers the flow is laminar and symmetric.

With increasing Reynolds number the flow becomes unsteady and oscillatory modes are excited. Figure 4.2 shows the time evolution of the column density of a collimated flow with $Re=1000$ and $Ma=0.9$. The flow is symmetric for the first 2000 time steps. Then, a second vortex is excited and the flow starts pulsating. As more vortices appear, the flow breaks up into individual filaments. The interaction between the vortices finally produces an overall asymmetric flow structure. To show the complicated three-dimensional patterns, I have calculated a 3D volume rendering image of the tracer density for a shear flow with $Re=1500$ and $Ma=0.9$ (Figure 4.3). The rendering opacity has been chosen such that the knots and filaments are clearly seen.

At Reynolds numbers around 1000 the velocity components perpendicular to the main flow axis are large enough to produce substructure in the spectral lines. Figure 4.4 shows the spectra for the last time step of Figure 4.2. They have been calculated for a 45° projection angle. The velocity interval for each spectrum is four times the sound speed. Towards the flow's central region the spectra are broad and at the border between background gas and inflow they are partly double peaked. Similar structure is seen over the whole range of simulated Mach numbers. However, below $Ma=0.6$ the distinct line structure vanishes due to the thermal line broadening.

At high Reynolds numbers the flow gets isotropically turbulent. The large scale filamentary structure become less distinguished and finally it completely disappears for Reynolds numbers above $\sim 10^4$. Instead the flow is spatially symmetric like in the laminar case but with a cone-like shape. Figure 4.5 shows an example of a flow at $Re=20000$. Due to the isotropic turbulence the resulting spectra are broad throughout the flow, but they do not exhibit distinct wing or double peak structure (see Figure 4.6).

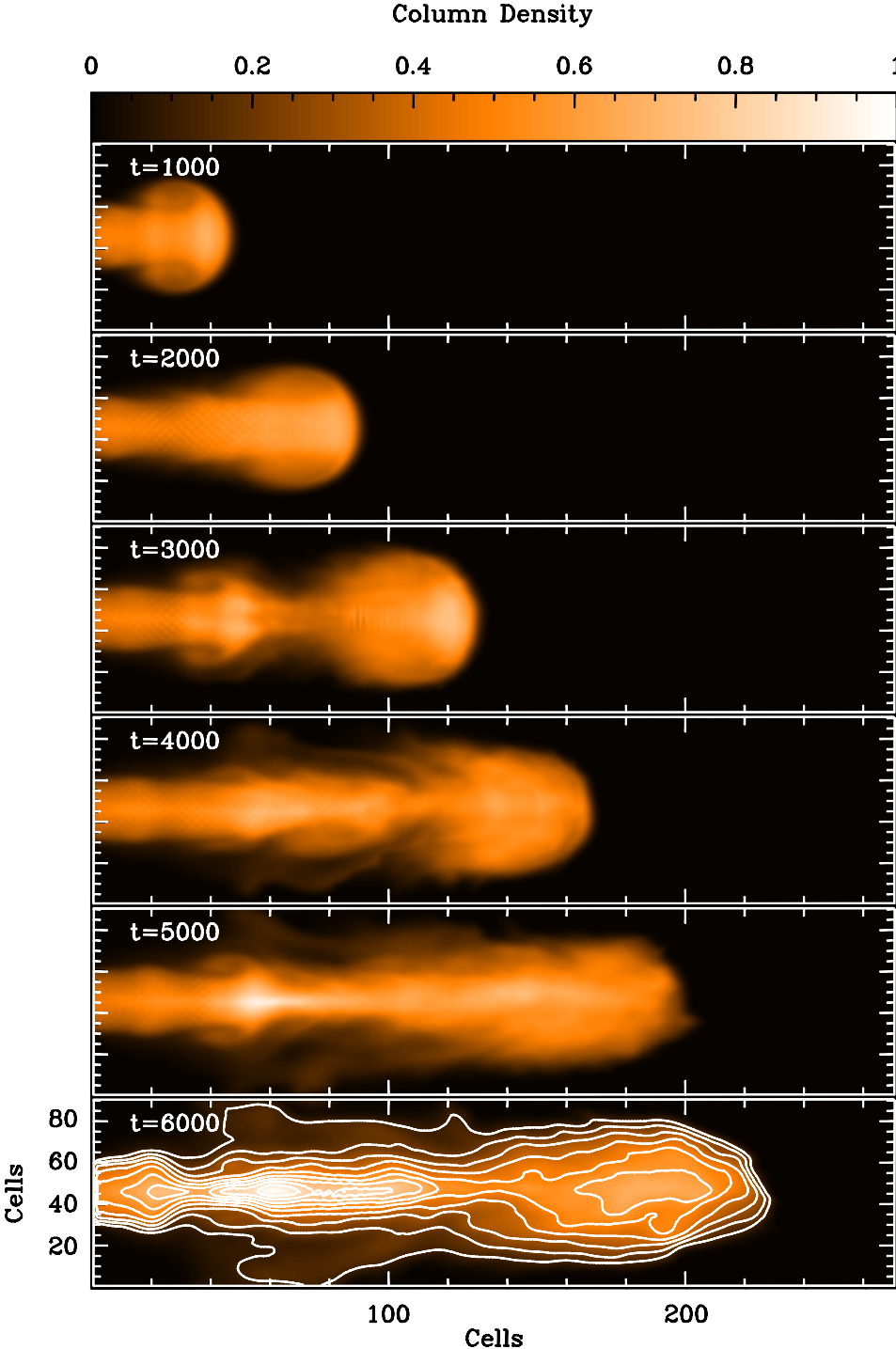


Figure 4.2: Time evolution of a collimated shear flow with $Re = 1000$ and $Ma = 0.9$. For the first 2000 time steps the flow is nearly symmetric. The small perturbations then grow non-linearly toward the large scale spatial asymmetries.

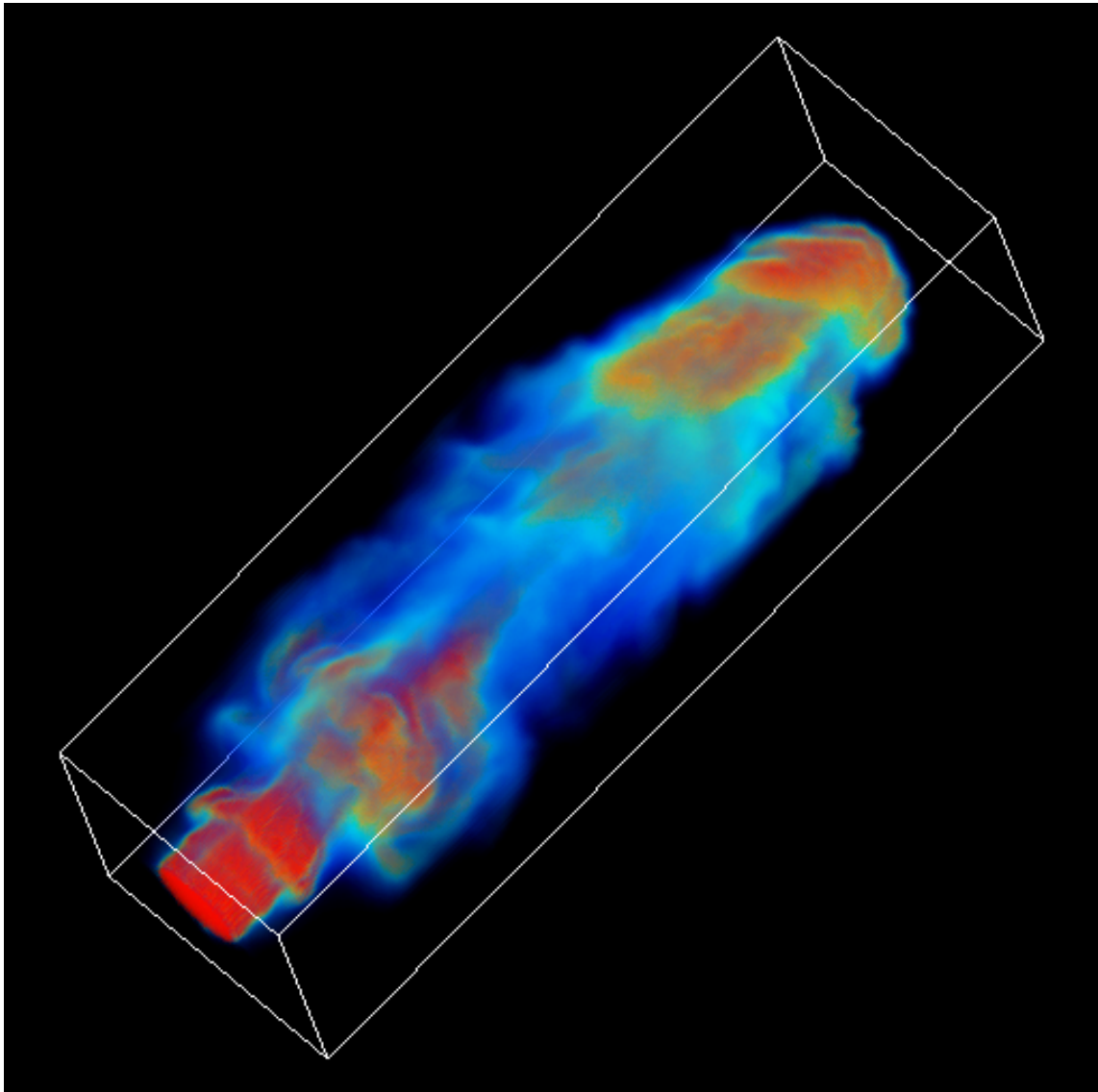


Figure 4.3: 3D volume rendering of the tracer density for a collimated shear flow with $Re = 1500$ and $Ma = 0.9$. The opacity and false colors have been selected to clearly show the knotty and filamentary structure which is seen only at intermediate Reynolds numbers between 500 and 5000.

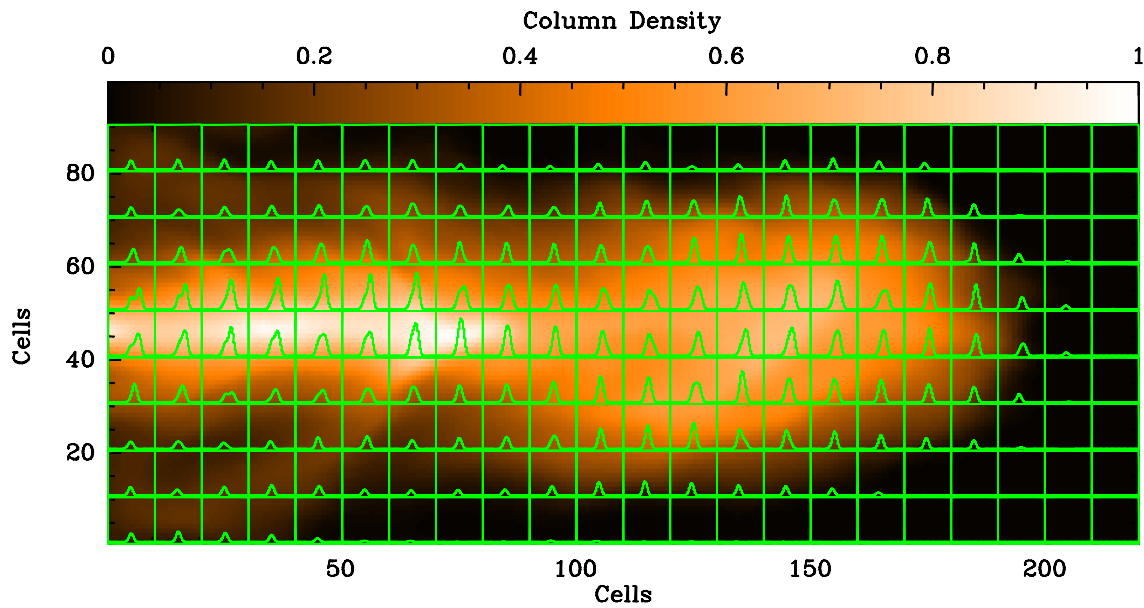


Figure 4.4: Model sulphur monoxide spectra for the last time step of Figure 4.2. The spectra have been calculated for a viewing angle of 45° relative to the flow axis. They are superposed on the column density map at the same projection angle. The velocity interval for each spectrum is four times the sound speed. Double peaked structures are seen at the border between the background gas and the inflow. Towards the central flow region the spectra are broad.

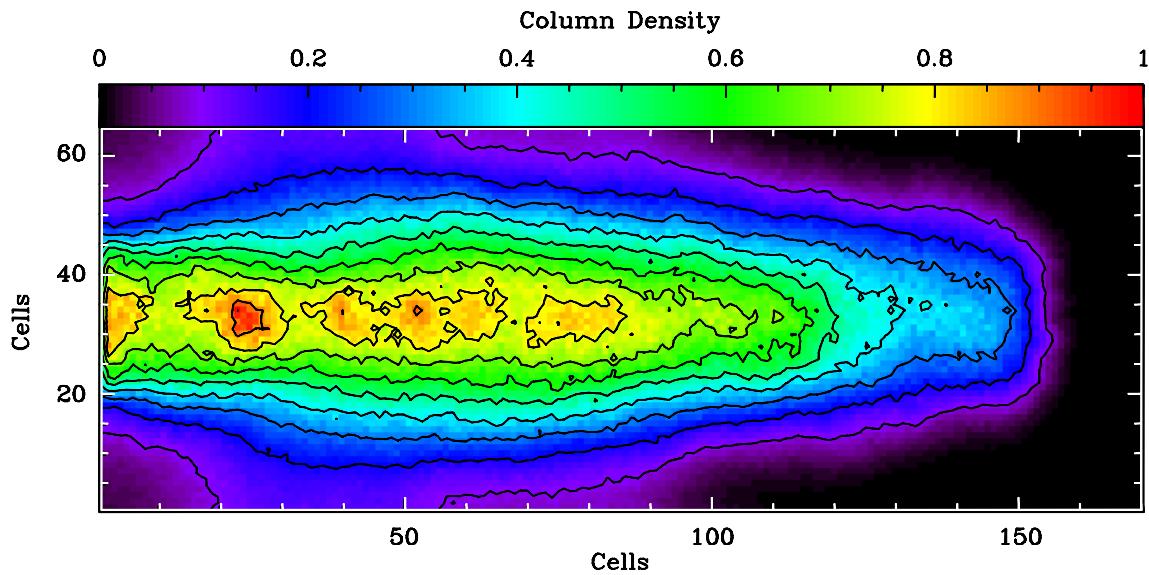


Figure 4.5: Column density of a collimated shear flow with $Re=20000$ and $Ma=0.6$. At high Reynolds numbers the flow becomes isotropically turbulent. No distinct clumpy and filamentary structure is seen.

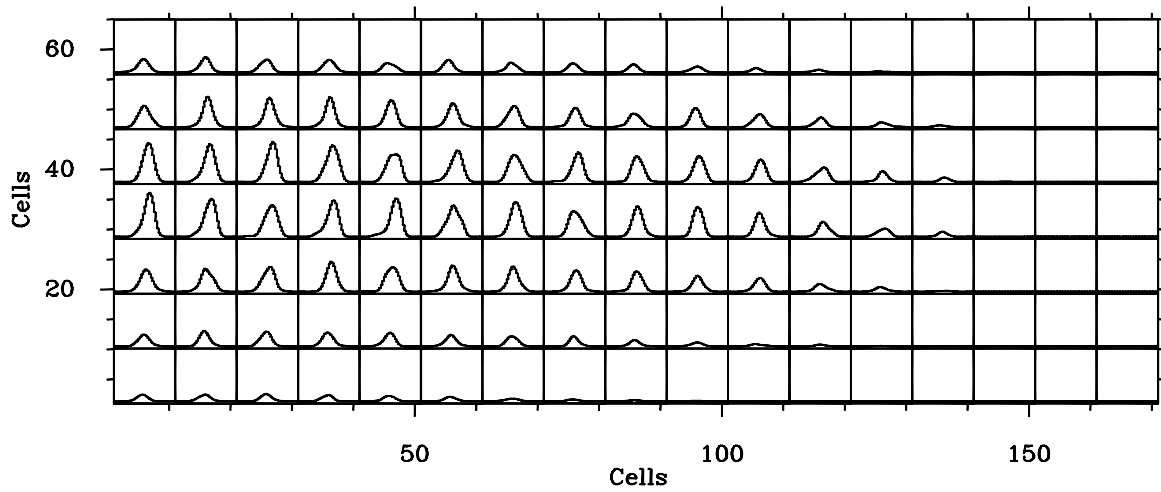


Figure 4.6: Model spectra for a collimated shear flow with $Re=20000$, $Ma=0.6$. The spectra at high Reynolds numbers are broad throughout the flow. They do not exhibit distinct double peak structure which is seen at lower Reynolds numbers.

4.2 Cometary Tails

The second set of simulations involves the motion of molecular clumps through an ambient medium. The kinetic energy of the flow may tear off parts of the cloud which eventually produce a turbulent tail behind the clump. In the present simulations the initial clump is not dissolved in order that the tail structure can be studied in detail. Again, I assume equal densities for both fluid phases. For simplicity I leave the clump position fixed while the background is moving. After initially setting the background velocity field, the density and velocity values in the first plane of the data cube are continuously updated to keep the gas flowing. To prevent any molecular gas to flow back into the cube, I have employed an absorbing plane at the opposite end of the cube. Periodic boundary conditions are assumed along each of the three cube axes. Similar to the shear flow simulations I have applied small random fluctuations of up to $\pm 10\%$ to the density and the velocity of the incoming stream in order to induce the instabilities. The definition of a Reynolds number for this type of flow is somewhat ambiguous since the typical velocity scale may either be the background value or the decelerated value just behind the clump. However, the relevant structure is seen at a distance of more than one clump diameter away from the initial cloud so that I will give Reynolds numbers based on the clump size and the background velocity.

The flow is laminar for a Reynolds number below 400. The spectra do not exhibit any special signature in that regime. Shear instabilities begin to develop at higher Reynolds numbers. Figure 4.7 shows a time sequence of a cometary flow with $Re=1500$ and $Ma=0.6$. The flow starts pulsating after around 5000 timesteps and then produces distinct clumps. The distance between neighboring clumps is roughly equal to the initial clump diameter. The three-dimensional structure of the tracer density field for last time step is shown in Figure 4.8. The fluffy structure around the individual knots is clearly seen.

The spectra at $Re=1500$ are thermal even for high Mach numbers. This is due to the partial permeability of the clump and the large scale background velocity field. Strong forces are required to build up velocity components perpendicular to the main flow direction. Very distinct velocity structure appears for Reynolds numbers above around 3000 (see Figure 4.9). Very narrow spectra are seen toward the initial clump. Behind the clump the spectra are broader and they exhibit wing structure due to the turbulent motion. The special distribution of lineshapes is independent of the Mach number. Only the absolute value of the linewidths changes. Below Mach numbers of 0.6 the components are too small to be seen in the thermally broadened spectra. The velocity structure also stays the same for higher Reynolds numbers up to the numerical limit. But above Reynolds numbers of 5000 no distinct clumps are seen in the isotropically turbulent tail. If more than one initial clump are placed into the background flow, then the individual tails interact non-linearly to produce more complex structure. Figure 4.10 shows a 3D volume rendered image of three clumps which have been grouped together. The tail structure is much more complicated than in the single clump case.

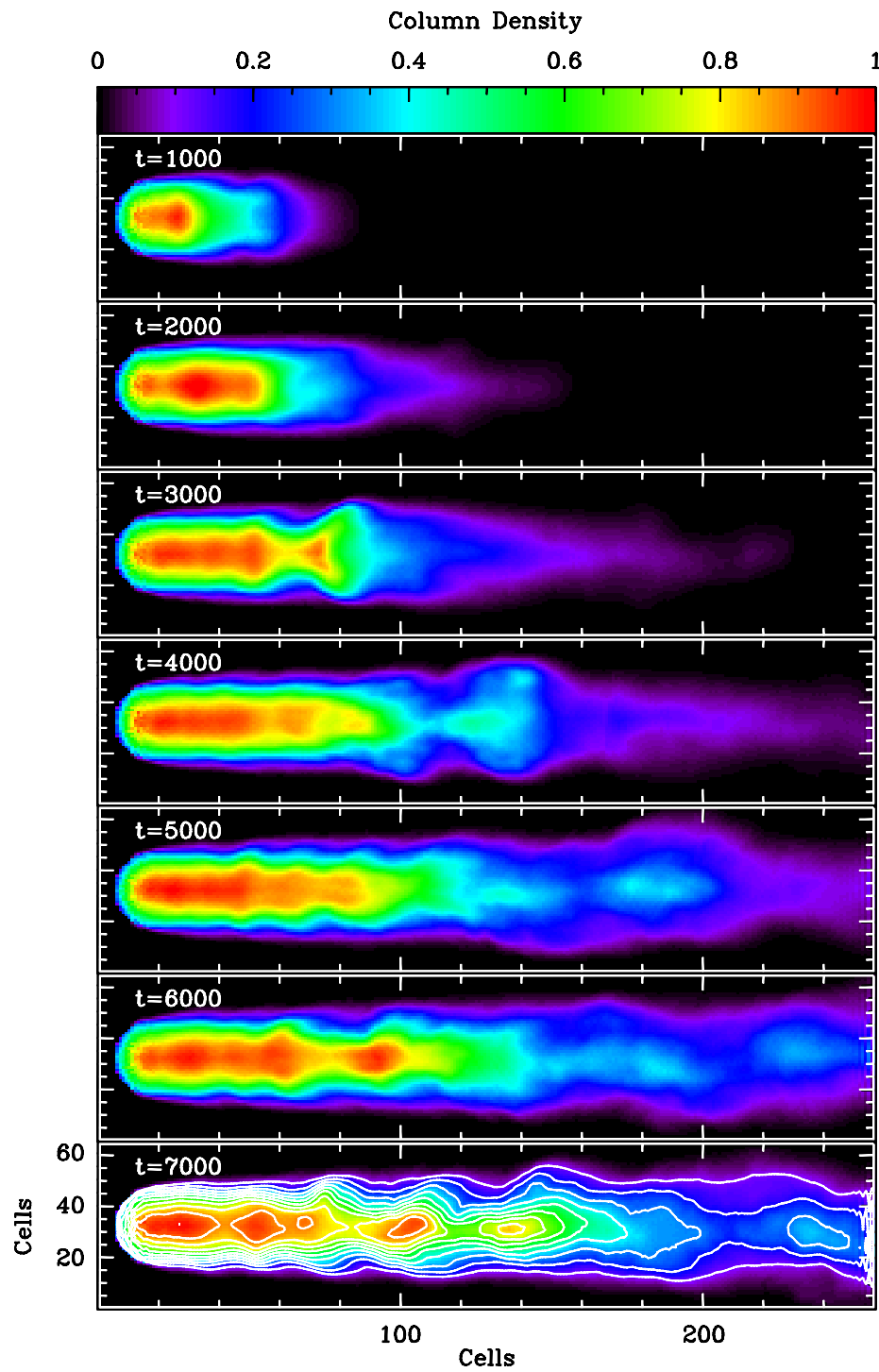


Figure 4.7: Time evolution of the development of a pulsating tail behind a dense clump with a Reynolds number of 1500 and a Mach number of 0.6. Each panel shows the column density perpendicular to the main flow axis. After around 5000 timesteps the flow starts oscillating. Later, individual clumps are produced.

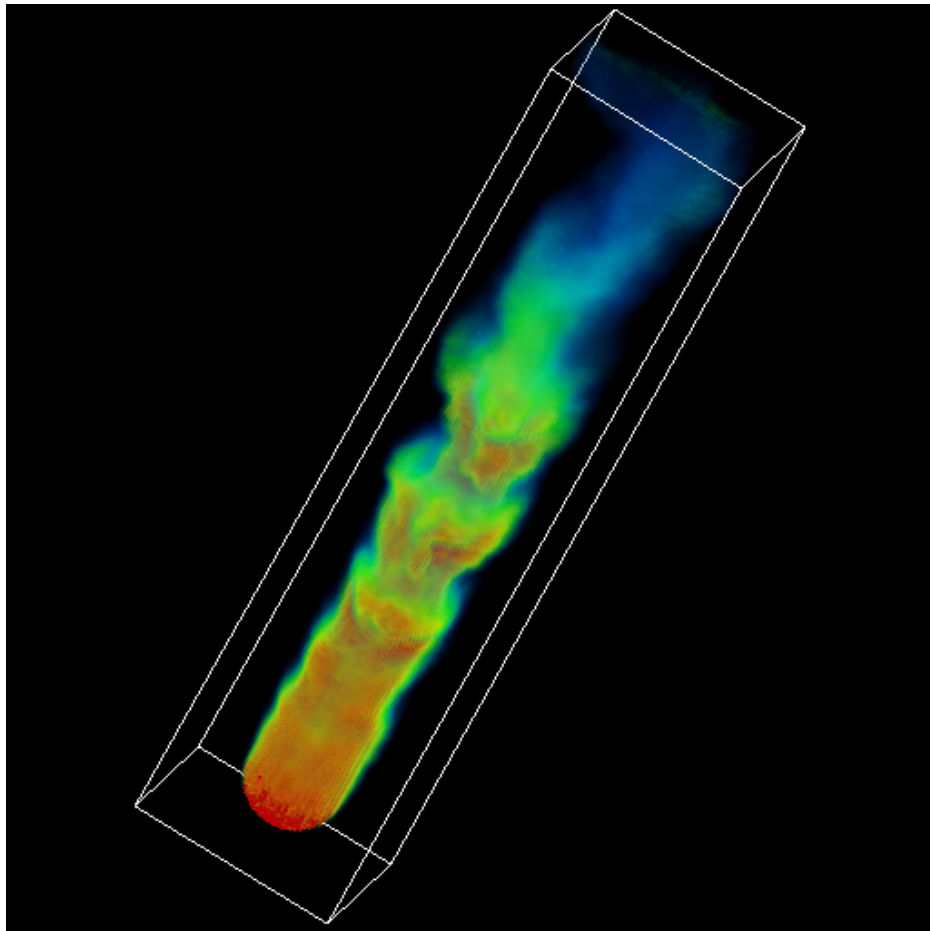


Figure 4.8: 3D volume rendering of the density field of the last timestep of Figure 4.7. This image clearly shows the fluffy structure around the distinct knots. The distance between neighboring knots is roughly equal to the diameter of the initial clump.

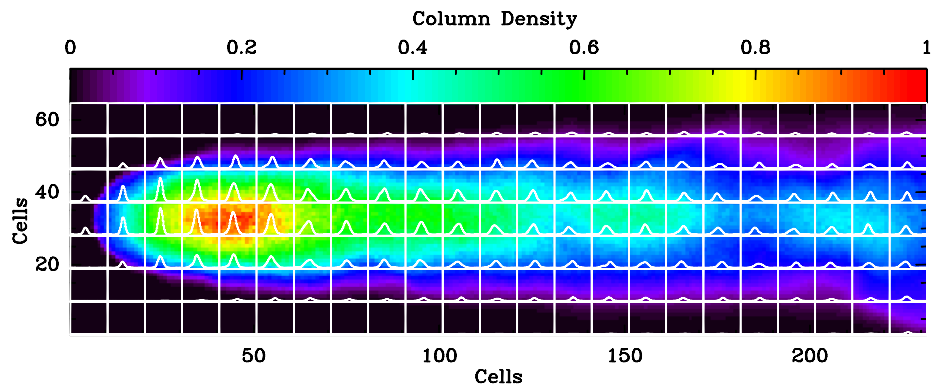


Figure 4.9: Model spectra of a cometary tail simulation with $Re=3000$ and $Ma=0.6$. The spectra are superposed on the column density map. The projection angle is 45° with respect to the main flow axis. Very narrow thermal spectra are seen toward the initial clump while the spectra are broader and asymmetric in the tail. This distribution is characteristic for this type of flow.

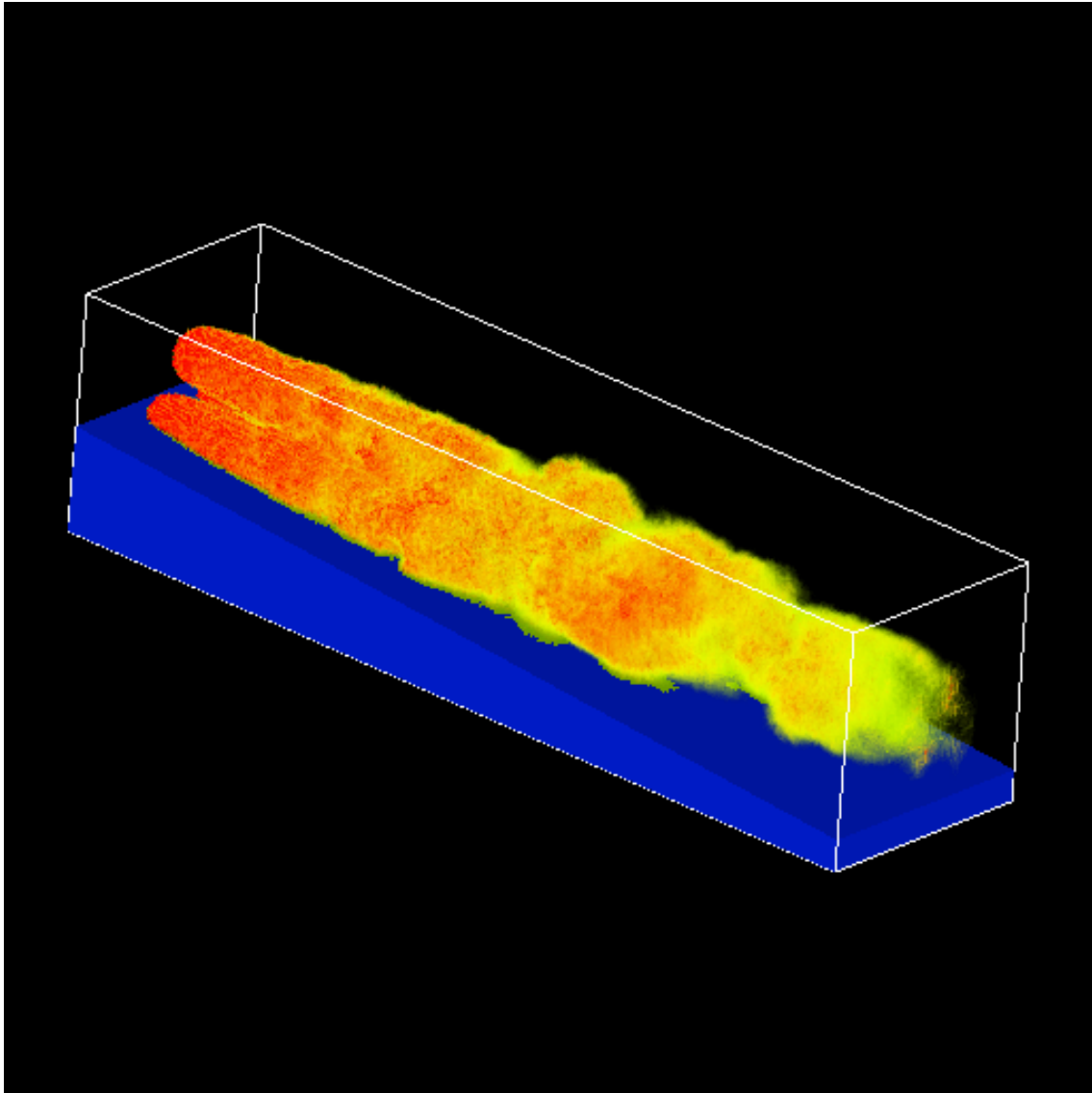


Figure 4.10: 3D volume rendering of the turbulent flow structure behind three dense clumps. If more than one clump is grouped together, then the individual tails interact to produce increasingly complicated flow patterns.

4.3 Results

Two main conclusions are to be drawn from the simulations. (1) Distinct spatial and velocity structure is seen only for the transition between laminar and isotropically turbulent flow at Reynolds numbers between 500 and 5000 and (2) *subsonic* viscous shear flows are able to generate lineshapes similar to the ones observed toward interstellar cold dark clouds. The occurrence of well-defined structure in the transitional regime between the highly ordered laminar and the completely random turbulent patterns may be interpreted in the framework of the “Edge of Chaos”. This phrase had been coined by Packard (1988) and Langton (1990) who concluded from experiments with cellular automata that the storage capacity of a system is largest at the transition between two phases. Complex systems, such as the interstellar clouds, seem to exist only in narrow transitional regimes.

The rather low intermediate Reynolds numbers seem at first incompatible with the much higher values of around 10^7 derived from the physical parameters of dark clouds. However, when taking magnetic fields into account, the effective Reynolds numbers may be much lower if the coupling between the magnetic field and the gas is strong enough. Myers and Kheronsky (1995) estimated the magnetic Reynolds number, Re_M , for several components of the interstellar medium. Re_M is defined by

$$Re_M \propto Lv\rho T^{0.5} B^{-2} x_e \quad (4.5)$$

where ρ is the gas density, T is the kinetic temperature, B is the magnetic field strength and x_e is the electron fraction due to cosmic ray ionization and photoionization through star light. Adopting magnetic field strengths around $15\mu G$ and electron fractions of $\sim 10^{-5}$ Myers and Kheronsky derive Re_M values of the order $10^{1.2}$ to $10^{3.4}$ for dark clouds. This is in the range that has been predicted from the simulations. Magnetic fields may thus play an important role in the dynamics of the most quiescent part of the interstellar medium.

Chapter 5

Observations

To compile a database of molecular cloud observations for the comparison with theoretical models we (J. Schmid-Burgk and D. Muders) have begun to map a number of regions, either quiescent or actively star forming, with the MPIfR 100m radio telescope at Effelsberg. We used the relatively new receiver for the 26 GHz to 36 GHz band as well as the 1.3 cm maser receiver to obtain mostly sulphur monoxide (SO) and ammonia (NH₃) data. The ground transition of sulphur monoxide (SO 1₀ – 0₁) proved to be a good tracer of spatially extended dark cloud structure (Schmid-Burgk and Muders 1994).

5.1 Lynds 1512

For the comparison with the model calculations I have selected one source, the dark cloud L1512 (Lynds 1962), which is located approximately 140 pc away (Elias 1978) in the Perseus Taurus region at $\alpha_{1950} = 5^{\text{h}}0^{\text{m}}54.4^{\text{s}}$ $\delta_{1950} = 32^{\circ}29'0''$ (ammonia peak position by Myers and Benson (1983)). The mean LSR velocity of L1512 is 7.1 km s⁻¹. Our own Effelsberg observations of the ammonia (1,1) inversion line exhibit one dense core peaking at an offset of (-30'', 30''). The NH₃(2,2) line is not seen. Therefore, the gas temperature in this dense region must be of the order 10 K. This is consistent with the value given by Myers and Benson. H₂ gas densities have been estimated by Cox (1995). He applied an LVG formalism on C₃H₂ observations and derived approximately 10⁵ cm⁻³ toward the peak position of the dense core. No IRAS sources are associated with L1512 and the ammonia linewidths are barely above the respective thermal value. Therefore, L1512 is thought to be one of the most quiescent dark clouds with no evidence of ongoing star formation. Yet, it exhibits spatial and velocity structure as will be shown below. It is thus an ideal candidate to search for the basic structure forming flows in the interstellar medium.

5.1.1 Sulphur Monoxide Observations

The L1512 region has been mapped in the ground transition of sulphur monoxide (SO 1₀ – 0₁) at 30.001539 GHz using the 100m telescope at Effelsberg. At 30 GHz the FWHM of the beam is 30''. The spectra were taken with the autocorrelator split into two parts of 512 channels, each with 1.56 MHz bandwidth. Thus, the velocity resolution is ~0.03 km s⁻¹. The spectra from both autocorrelator parts were co-added to get roughly 10% lower noise temperatures. Pointing was

checked regularly on nearby continuum sources. The cross scans have also been used for calibrating the sulphur monoxide data to a main beam brightness temperature scale.

For the first time at Effelsberg we used the “On-The-Fly” mapping method for spectral line observations. The telescope is scanning continuously along the columns or rows of the maps while dumping the spectra at given times. This saves up to 30% of real observing time since the telescope does not have to stop between the individual grid points. We used “On-The-Fly” mapping to first coarsely search for emission in large areas and then thoroughly map the regions of interest. To minimize beam distortions, the distance between two grid points must be smaller than the beam width. We used a scanning velocity of 30'' per minute and dumped a spectrum every 30 seconds, i.e. spatially every 15 seconds of arc. These fully sampled maps have been done several times for each region with changing scanning directions (either Right Ascension or Declination) to check for pointing accuracy and calibration consistency. We observed mainly by frequency switching with a splitting frequency of 0.4 MHz, roughly one fourth of the total bandwidth. This value ensured ample separation of positive and negative signal and avoided edge effects. Compared to position switching we gained about a factor of two in observing time.

We have taken more than 16000 individual spectra distributed over an area of 600'' \times 900''. Some automatization in the reduction process was therefore necessary. In the first step all bad weather spectra have been discarded by using only observations with system temperatures below \sim 400 K. From the remaining spectra a baseline of at most first order has been subtracted. Bad channels, ripples and autocorrelator failures have been detected via Fourier analysis. Calibration and pointing deviations for maps of the same region were typically less than 20% which is in the range of the receiver / backend accuracy. Therefore, no large scale corrections were necessary (note that this is valid over three wintertime observing periods!). The mean total integration time per point after co-addition is about 4 minutes. For the final maps we added the spectra of four neighboring points of the fully sampled map to lower the r.m.s. noise by another factor of two.

5.1.2 Sulphur Monoxide Maps

The sulphur monoxide spectra are shown in Figure 5.1. The plot contains only one spectrum per beam to avoid overcrowding. The velocity range for each spectrum is 6.17 to 7.88 km s⁻¹ and the maximum main brightness temperature is 2.75 K. The size of L1512 is 0.9 \cdot 10¹⁸ cm along right ascension and 1.7 \cdot 10¹⁸ cm along declination. Very narrow unperturbed spectra are found at the southern edge of the dark cloud. The smallest FWHM linewidths in that region are around 0.15 km s⁻¹. Towards the north the SO spectra are broader (up to 0.4 km s⁻¹) and they have asymmetric lineshapes.

The velocity integrated intensity shows the clumpy structure of L1512 (Figure 5.2). Several clumps of different size are located in a tail-like structure roughly along a south-west to north-east axis. The southernmost clump has a sharp edge. No distinct sulphur monoxide emission is seen toward the ammonia peak position at (-30'', 30''). This indicates that SO traces a spatially extended medium with physical conditions rather different from those seen with ammonia. Therefore, the temperature and hence the local sound speed derived from the ammonia data cannot be used for the comparison with the dynamical models. To estimate the physical parameters, I have used the spectra of the southern clump in L1512. Their symmetric unperturbed structure suggests that the linewidths are near the local thermal value. Using equation 4.4 with the smallest linewidth of 0.15 km s⁻¹ I derive $T = 20$ K and $c_{s,H_2} = 0.35$ km s⁻¹.

The velocity structure of L1512 is revealed by the channel maps (Figure 5.3). Remember that the cloud's systemic velocity is 7.1 km s^{-1} . At blueshifted velocities ($6.45\text{--}6.75 \text{ km s}^{-1}$) there is a distinct streamer-like object. Its head is located at $(-40'', 130'')$. Its tail points toward the north-west. At redshifted velocities ($7\text{--}7.36 \text{ km s}^{-1}$) an elongated structure with three separate large clumps emerges. Both structures overlap in the intermediate velocity range. To get a clearer view of the kinematic structure of L1512, I have constructed a "true color" image (Figure 5.4). The Doppler shifted velocity has been coded as blue and red colors while the intensity corresponds to the line brightness temperature. Thus, the true color plot simultaneously shows spatial and velocity structure. Here, the velocity interval from 6.7 km s^{-1} to 7.2 km s^{-1} has been used. Again, the redshifted clumpy pattern appears on the eastern side of the source. The blue streamer's distinct velocity is clearly seen. Its head is located at the inner corner of the redshifted emission region. The spatial coincidence of both structures leads to the broad and double peaked spectra (see Figure 5.1). Both tails, red- and blueshifted, meet at the northern edge of the map.

5.1.3 Palomar Plate

The L1512 region has also been inspected on the red Palomar plate contained on CD-ROM¹². To enhance the dark cloud contrast, the stars had to be removed from the image. To this end, I have marked all parts above a photographic density of 0.53 which was the limit where stars started to become visible. I then calculated the mean intensity and r.m.s. of the remaining plate pixels' intensities. These values have been used to fill the "star holes" with white noise. Finally, the data have been resampled to the SO map's resolution to get a smoother image. The result is shown in Figure 5.5. The contours of the integrated sulphur monoxide map (Figure 5.2) are superposed.

The optical plate reveals two large "twisted" drop-like clumps. The southern clump is denser than its northern counterpart. The clumps are surrounded by bright filamentary emission which extends further outwards in four different directions. The filaments are probably seen as a result of scattering star light by small amounts of dust grains. The SO emission follows the general geometrical outline of the extinction pattern. However, the SO maxima do not coincide with the densest regions. On the contrary, they mostly appear at the edges of the dark clumps. Remarkably, the SO emission extends along the filamentary tracks. Redshifted SO emission is seen on the lower western and the northern filament while the blueshifted tail splits up into two paths on the upper western and the northern filament. Weak SO emission seems to extend also along the eastern filament.

¹²Based on photographic data of the National Geographic Society – Palomar Observatory Sky Survey (NGS-POSS) obtained using the Oschin Telescope on Palomar Mountain. The NGS-POSS was funded by a grant from the National Geographic Society to the California Institute of Technology. The plates were processed into the present compressed digital form with their permission. The Digitized Sky Survey was produced at the Space Telescope Science Institute under US Government grant NAG W-2166.

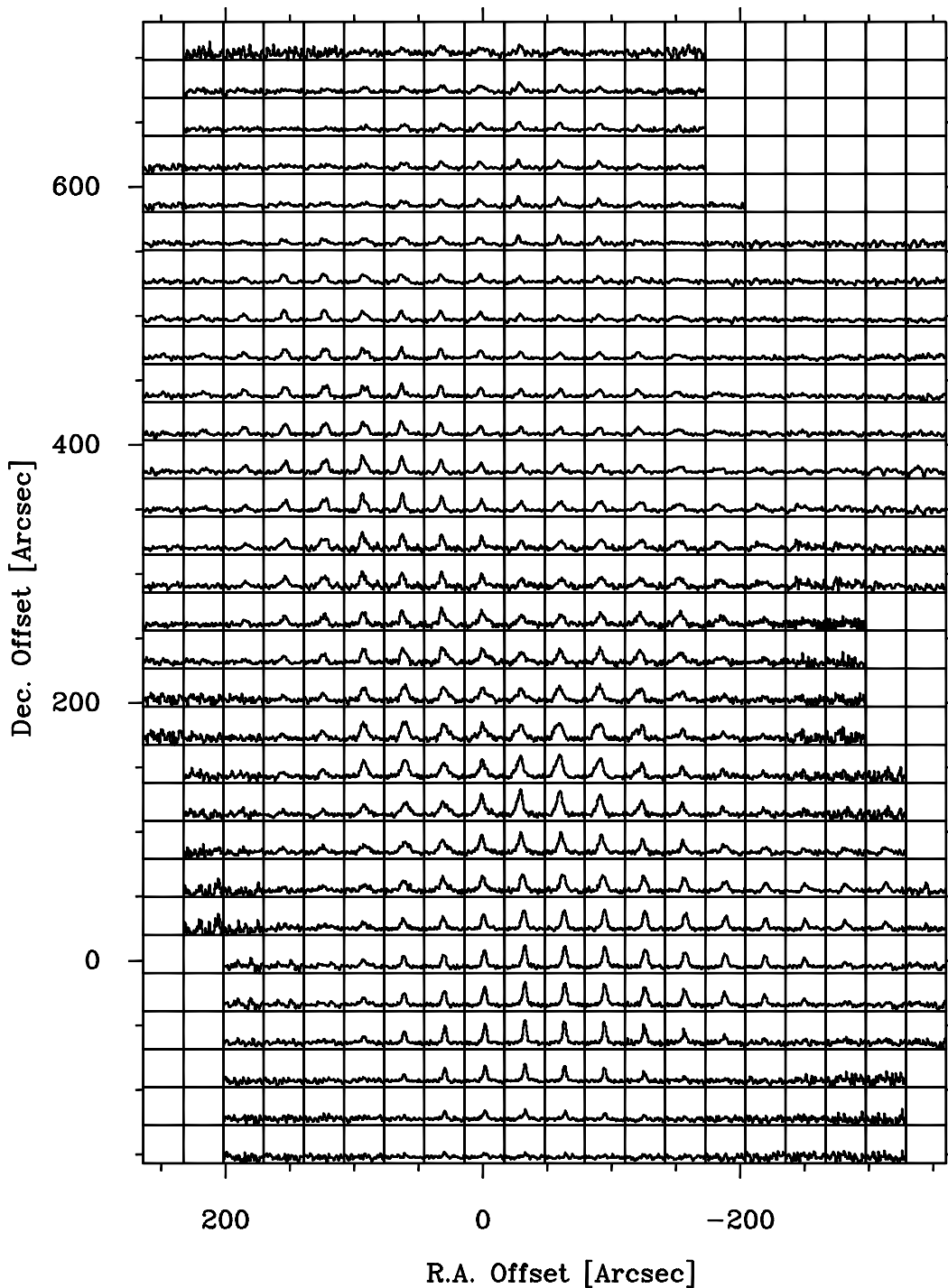


Figure 5.1: *SO* $1_0 - 0_1$ spectra toward L1512. The velocity range for each box is 6.17 to 7.88 km s^{-1} . The plot shows only one spectrum per beam to avoid overcrowding. Some edge spectra exhibit a rather low signal to noise ratio due to insufficient observing time. The general structure of L1512 appears to be elongated roughly along a south-west to north-east axis. The southernmost spectra are very narrow (0.15 km s^{-1}). Towards the north the spectra are broader and they exhibit asymmetric line shapes and double peaks.

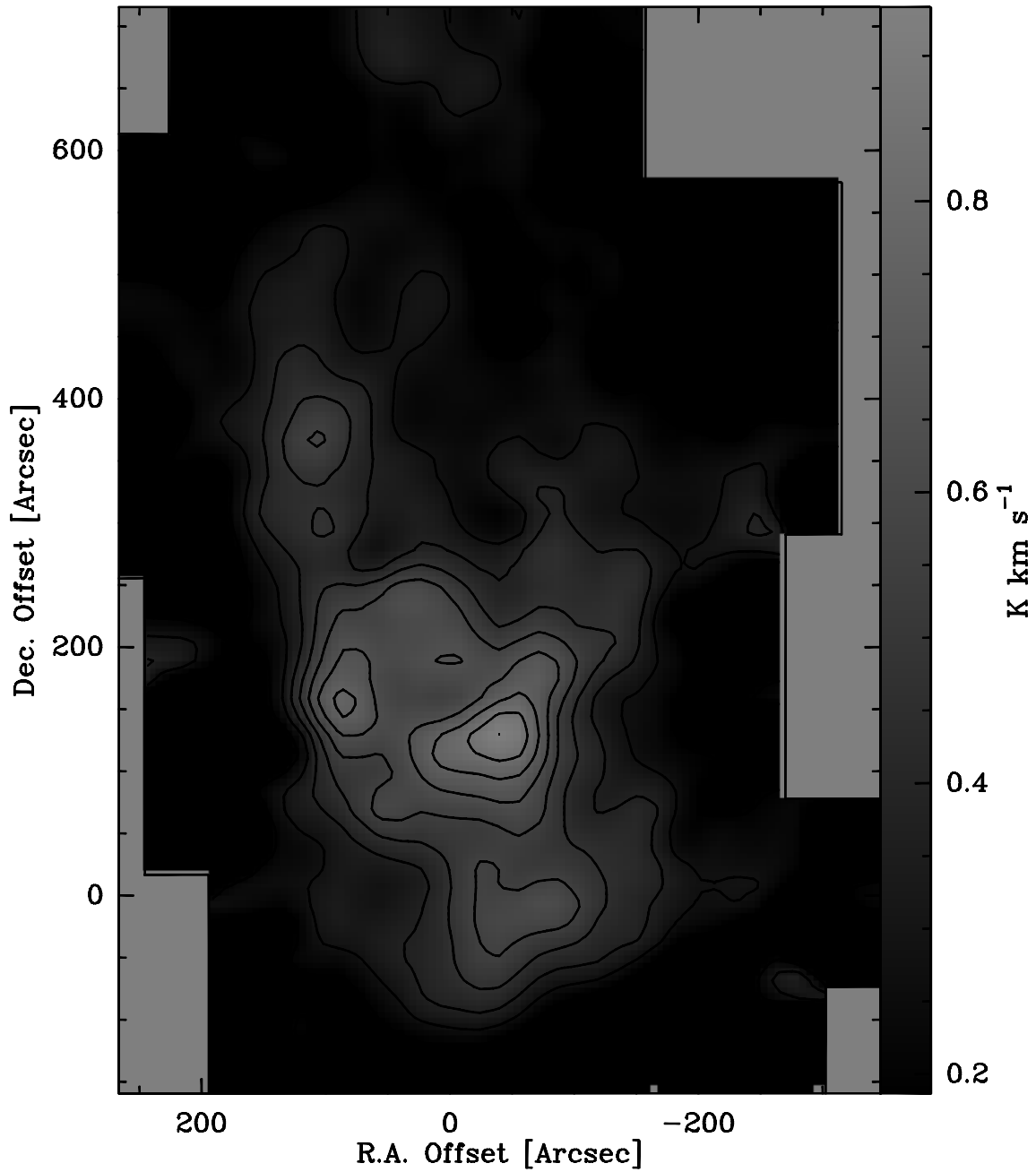


Figure 5.2: *Integrated SO $1_0 - 0_1$ intensity toward L1512. The contours and grey scale start at 0.2 K km s^{-1} . Contour steps are in increments of 0.1 K km s^{-1} . A tail of clumps of different size extends from the south to the north. Note the sharp edge of the southernmost clump.*

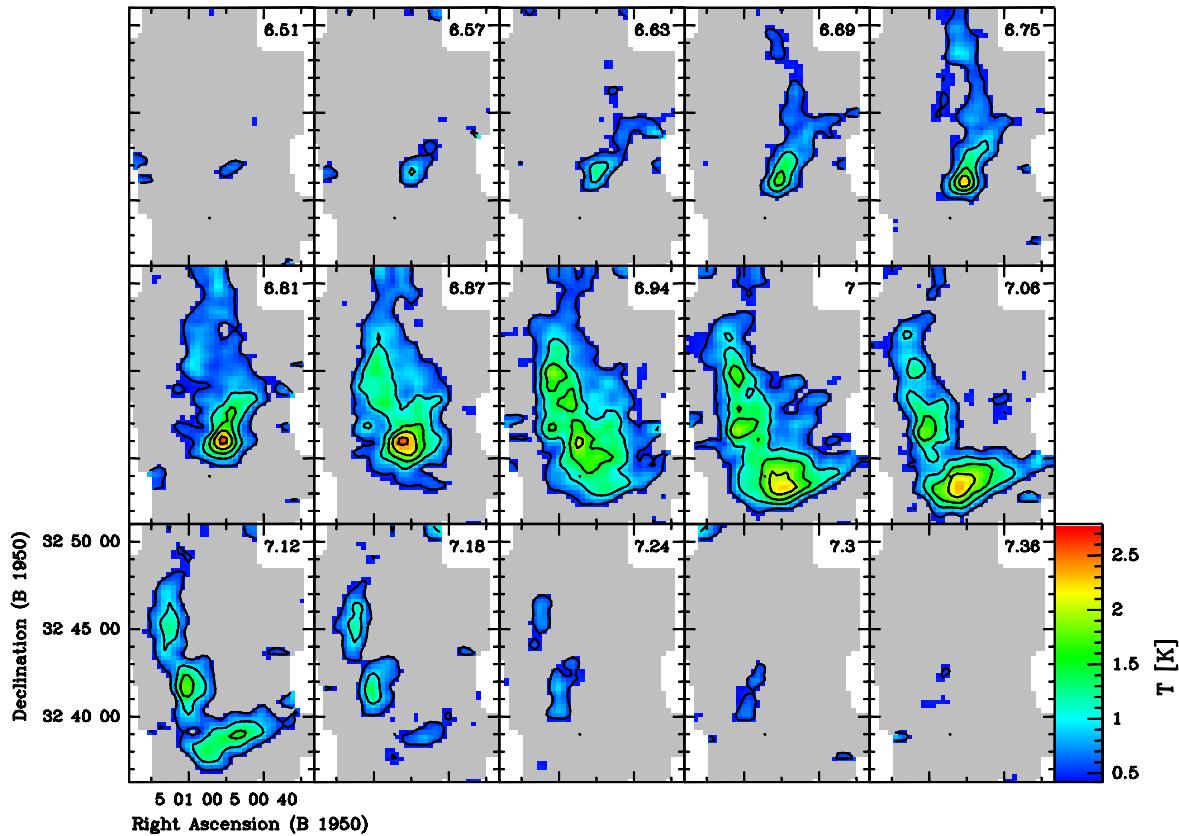


Figure 5.3: Channel maps of $\text{SO } 1_0 - 0_1$ emission toward L1512. Each bin is 0.06 km s^{-1} wide. Center velocities are marked in the upper right corner in km s^{-1} . The contours have been drawn in steps of 0.5 K starting at 0.5 K . The greyish background delineates the extent of the SO map. At blueshifted velocities a distinct streamer-like object is seen. Its head is located at an offset of $(-40'', 130'')$. The redshifted SO emission exhibits a clumpy tail emerging from the very quiescent southern clump.

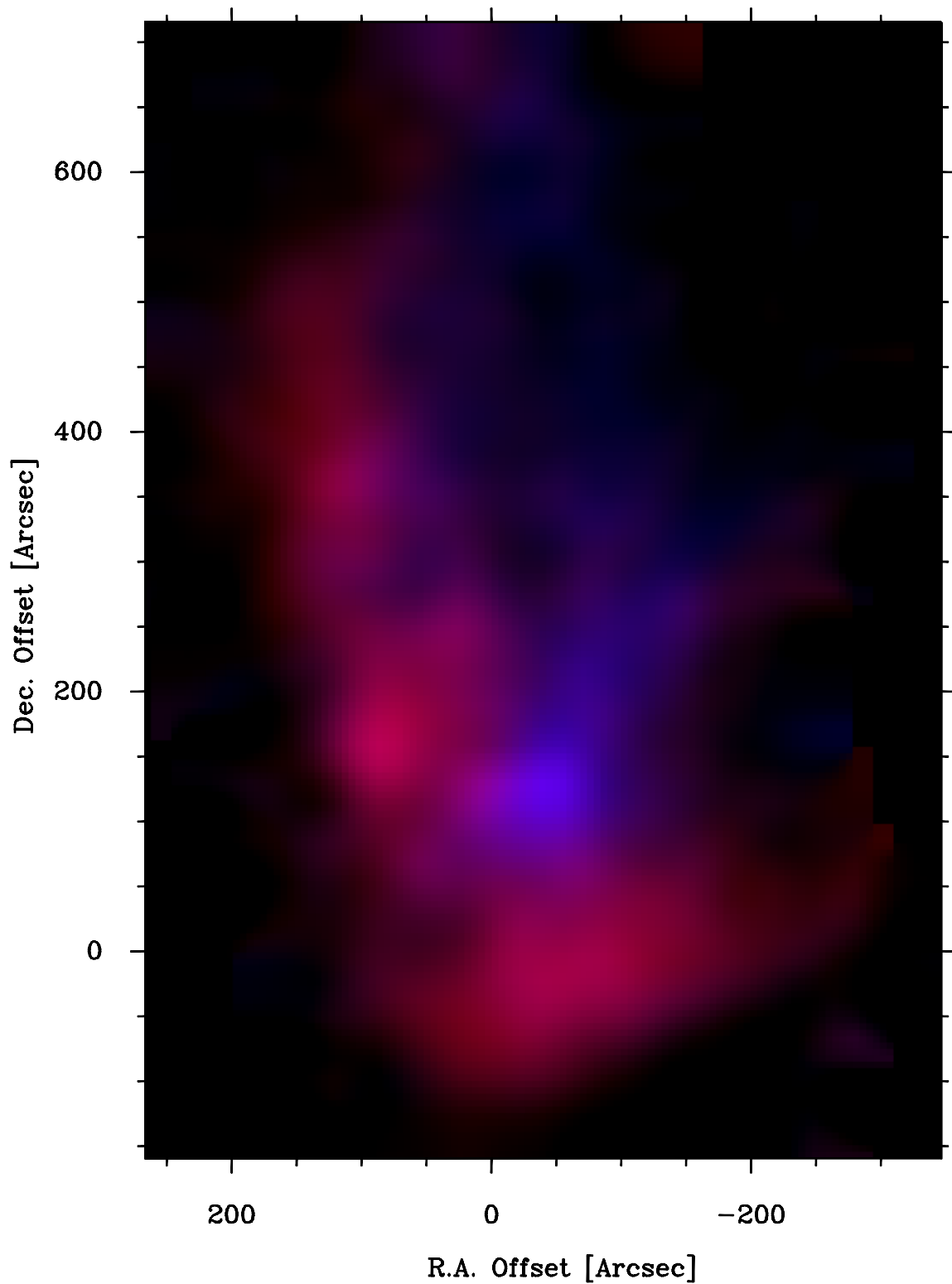


Figure 5.4: True color plot of SO 1_0-0_1 emission toward L1512. The colors have been calculated according to the Doppler shifted velocities along each line of sight. Blue is at 6.7 km s^{-1} , red at 7.2 km s^{-1} . The SO intensity is coded by the color brightness. True color plots allow the simultaneous representation of spatial and velocity structure.

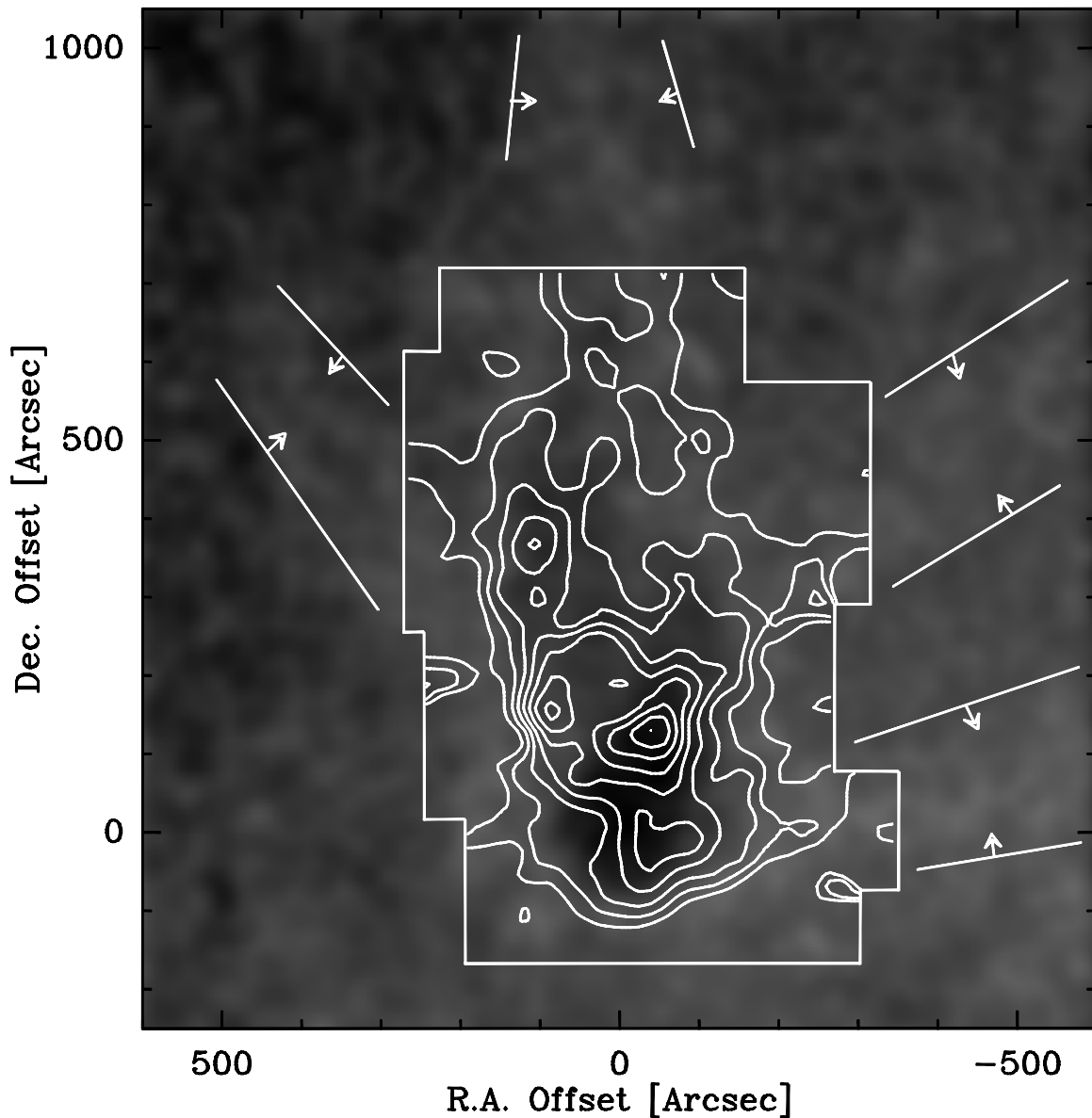


Figure 5.5: Red Palomar plate of the region around the dark cloud Lynds 1512. The stars have been removed to enhance the dark cloud's contrast. The original image has been smoothed to the SO map's resolution of $30''$. The contours of the integrated SO intensity from Figure 5.2 have been superposed. The Palomar data exhibit two large drop-like clumps. Those clumps are surrounded by bright filamentary emission. At four different positions the filaments extend further outwards into the ambient medium (see the white line drawings in the figure). The SO emission follows the general extinction pattern. However, the SO maxima are mostly located on the edges of the clumps. Remarkably, the SO emission seems to follow the optical filaments.

5.2 Simulation versus Observation

The sulphur monoxide spectra of L1512 show a velocity structure that is typical for cold dark clouds. The linewidths are at most a few times the thermal value and the line shapes are mostly asymmetric. The hydrodynamical simulations (see chapter 4) have shown that such a structure may be generated by *subsonic* turbulent shear flows at Mach numbers between 0.6 and 0.9 and at rather low Reynolds numbers of the order 500 to 5000. I interpret the transition of narrow bright spectra in the south of L1512 to the broader spectra in the north as a dynamical evolution originating from the southern clump with its unperturbed structure. Shear forces tear off parts of the cloud and produce the turbulent tail structure while the clump moves through the ambient medium in roughly southerly direction. The simulated spectra for such a hydrodynamical interaction at a Mach number of 0.6 are shown in Figure 5.6 at a viewing angle of 45° relative to the main flow axis. Note that the systemic velocity difference along the whole tail is only one fourth of the sound speed. This is due to the partial permeability of the model clump at the tail's head. The relative velocities between the clump and the ambient medium are thus lower than $0.6 c_s$. In L1512 the velocity difference is $0.1 \text{ km s}^{-1} = 0.29 c_s$. This is consistent with the model prediction.

To produce such a tail, the clump in L1512 must move with a velocity of the order 0.21 km s^{-1} . Thus, the dynamical age of L1512 is around $1.1 \cdot 10^6$ years. The hydrodynamical Reynolds number of L1512 can be estimated from equation 4.2. It is of the order $3 \cdot 10^6$ assuming an H_2 density of 10^4 cm^{-3} and a typical clump diameter of $2 \cdot 10^{17} \text{ cm}$. It is two orders of magnitude higher than the model prediction. This may indicate that magnetic fields are dynamically relevant since the magnetic Reynolds number for interstellar dark clouds is in general lower than the respective hydrodynamic Reynolds number (Myers and Khersonsky 1995). If L1512 is magnetically dominated then equation 4.5 predicts a magnetic field strength of the order 4 to $14 \mu\text{G}$ assuming cloud ionization through cosmic rays only. Additional photoionization through ultraviolet star light would lead to a slightly higher field strength.

The described model cannot account for the blue streamer and the filaments seen in sulphur monoxide. The comparison with the Palomar data indicates that additional effects on the clump "surfaces" may play an important role since sulphur monoxide emission is nearly always seen at the edges of the dark clouds. Depending on the detailed clump distribution, the main flow might be partially redirected so that we observe different radial velocities. In the case of the filaments dust and gas would be reflected and would protrude into the ambient medium along the surface tangents. However, there are two arguments against this model. Firstly, there is no significant velocity gradient along the filaments and secondly, it is difficult to imagine really "hard" clump surfaces. The interaction of the flow with an embedded magnetic field would be more realistic.

One might also argue that the optical filaments are signs of Mach cones. The projected full opening angle of roughly 90° predicts a Mach number of larger than 1.4. This picture would also answer the question why sulphur monoxide is seen at all since it is believed to be produced mainly through magneto-hydrodynamical C-type shock interaction (Pineau de Forêts et al. 1993). However, the very quiescent spectra of the southern clump then pose a new puzzle because there one would expect highly disturbed structure.

Concluding, I propose the cometary tail model to explain the overall velocity structure of L1512 with the distinct distribution of narrow and broad spectra. To explain the details such as the blue streamer and the optical filaments more observational data from other molecular transitions, as well as better optical or infrared images, are necessary.

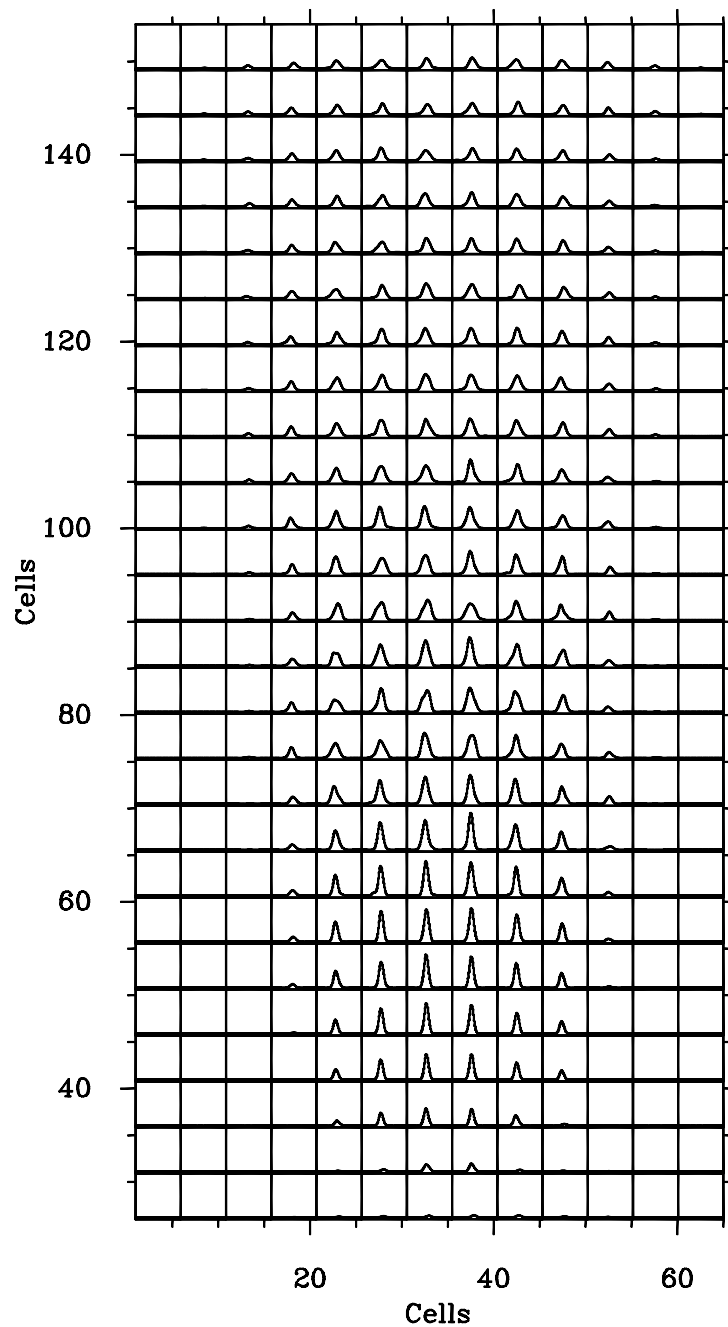


Figure 5.6: Model sulphur monoxide spectra of a cometary tail with a Reynolds number of 3000 and a Mach number of 0.6 at a projection angle of 45° . The velocity interval for each spectrum is four times the local sound speed. The transition from narrow spectra in the head toward the broader spectra in the tail is a distinct signature of a cometary flow. The velocity gradient across the tail is only one fourth of the sound speed since the main clump is partially permeable. The same structure is found in the sulphur monoxide data of L1512 (see Figure 5.1).

Chapter 6

Summary and Conclusion

The focus of this thesis work has been the investigation of the physical processes that create the clumpy and filamentary structure in cold interstellar molecular clouds. The prevalent gas flows are supposedly turbulent so that their detailed spatial and velocity structure can only be studied by numerical calculations. In this thesis I have introduced the recently developed “Lattice Boltzmann Method” (LBM) as a new tool to perform computational fluid dynamics. This is, to my knowledge, the first astrophysical application of the LBM. The “Lattice Boltzmann Method” calculates the evolution of particle packets that move with *discrete* velocities on a lattice. The simulation of the microscopic gas structure automatically guarantees global conservation laws and allows the implementation of arbitrarily complex objects. The LBM is perfectly suited for the application on parallel or clustered computers, a technology that currently emerges as the most promising way to provide the necessary performance to tackle long-standing problems like the simulation of three-dimensional turbulent flows.

As part of my thesis I have developed a three-dimensional parallel “Lattice Boltzmann” Navier-Stokes solver based on the “D3Q15” methods by Qian et al. (1992) and Chen et al. (1993) and the fourth order corrections by Chen et al. (1994). I have improved the numerical stability by introducing a selective viscous damping method which prevents the growth of large velocity gradients that would eventually lead to a numerical collapse. It is now possible to simulate three-dimensional flows with Mach numbers of up to 0.9 and at Reynolds numbers of up to $10^{4.5}$. I have added a second miscible fluid to model the molecular hydrogen and the tracer molecules, the two main components of dark clouds, separately. The code has been first parallelized for clusters of individual workstations using the PVM (Parallel Virtual Machine, Beguelin et al. (1991)) and ADAPTOR (Automatic DATA Parallelism TranslatOR, Brandes (1993)) packages. For the simulations I have used the three most powerful workstations (HP 735+) currently available at the “Max-Planck-Institut für Radioastronomie” (MPIfR) in Bonn. In parallel, they have a peak performance of 150 MFLOP and a main memory of 420 MByte. This allowed to simulate cube sizes of up to 140^3 voxels within 2 to 3 days CPU time.

However, for the systematic exploration of the parameter space the results must be available in shorter time. Therefore, I applied for computing time on the massively parallel mainframe “Connection Machine 5” (CM-5, TMC (1993)) at the “Gesellschaft für Mathematik und Datenverarbeitung” (GMD) in St. Augustin near Bonn. The 64 node at the GMD has a peak performance of 8 GFLOP and a main memory of 2 GByte. I have ported the code to the data parallel programming language CM FORTRAN. The PVM program structure has been changed to a slicewise algorithm that proceeds plane by plane through the 3D data cubes. Thus, the generation of temporary arrays is minimized and the combined vector parallel architecture of the CM-5 is fully

exploited while sufficient memory remains for the data. The CM-5 code was typically 10 to 15 times faster than the PVM solution, thus allowing for the completion of one run in a few hours.

I have used the LBM code to simulate collimated shear flows and cometary tails behind molecular clumps which move through an ambient medium. I have studied the dependence of the emerging spatial and velocity structure on the Reynolds and Mach numbers. The simulations show that distinct clumpy and filamentary structure is seen only for a small range of Reynolds numbers between 500 and 5000. *Subsonic* viscous shear flows with Mach numbers as low as 0.6 are capable of producing asymmetric line shapes or double peaks. The rather low Reynolds numbers seem at first incompatible with the values derived from dark cloud observations. The purely hydrodynamic dark cloud Reynolds numbers are of the order 10^6 to 10^7 . However, magnetic fields may lower the effective Reynolds number by several orders of magnitude if the coupling between ionized and neutral gas is strong enough. Myers and Khersonsky (1995) estimated the dark cloud magnetic Reynolds number to be of the order $10^{1.2}$ to $10^{3.4}$. The corresponding magnetic field strengths are around 10 to $30\mu\text{G}$. The occurrence of distinct clumps and filaments at intermediate Reynolds numbers, between the highly ordered laminar and the chaotic isotropically turbulent patterns, may also be interpreted in the framework of the "Edge of Chaos". This phrase had been coined by Packard (1988) and Langton (1990) to describe the tendency of complex systems, such as interstellar dark clouds, to exist only at the transition between different phases.

To compare the simulations with observed data, I have mapped the cold dark cloud Lynds 1512 with the MPIfR 100m radio telescope at Effelsberg. L1512 does not exhibit any sign of massive star formation. Therefore, it is thought to be one of the most quiescent dark clouds. I have obtained fully sampled maps of the ground transition of sulphur monoxide at 30 GHz. For the first time the "On-The-Fly" mapping method has been successfully used for spectroscopic measurements at Effelsberg. In that mode the telescope is moving continuously along the rows or columns of the map while the spectra are dumped at given times. Thus, the time for the stops between individual grid points is saved. Most of the spectra have been taken in frequency switching mode to gain about a factor of two in observing time. The resulting sulphur monoxide maps show a knotty tail-like structure with very narrow lines toward a large clump in the south and with broader lines in the tail. A distinctively blueshifted streamer is seen toward the north-west of the source. The sulphur monoxide spectra toward L1512 are representative for the class of cold dark clouds. The comparison with the simulations shows the close similarity between the observed and the theoretical spectra. The distinct transition from narrow to broad spectra is indicative of a turbulent tail evolution. The resulting dynamical age of L1512 is around 10^6 years. The magnetic field strength toward L1512 must be around 4 to $14\mu\text{G}$ to arrive at the predicted Reynolds numbers of a few thousand.

This thesis has demonstrated that the "Lattice Boltzmann Method" provides a new powerful tool to do computational fluid dynamics on parallel computers. In the future the scope of the method should be extended toward a working 3D thermo-hydrodynamics model that is capable of simulating supersonic flows. Thus, the more energetic interstellar events like bipolar outflows or stellar winds can be modelled. Magneto-hydrodynamics should be included since magnetic fields seem to play an important role for the dynamics of interstellar clouds. The calculation of the simulated spectra should include radiation transport for optically thick lines. New measures of complexity have to be developed to quantitatively compare simulations and observations. To this end, the existing theoretical work on complex systems should be taken into account. The comparison of radio data to the Palomar plate has shown that observations of dark clouds at optical wavelengths may provide new insights into the dynamics of these objects. Therefore, better optical observations of particular sources such as L1512 should be obtained.

Bibliography

- Adler, C., d’Humières, D., and Rothman, D. Surface tension and interface fluctuations in immiscible lattice gases. 1994, *Journal de Physique I (France)*, **4**, 29–46.
- Alexander, F.J., Chen, S., and Sterling, J.D. Lattice Boltzmann Thermodynamics. 1993, *Phys. Rev. E*, **47**, R2249.
- Appert, C. and Zaleski, S. Dynamical liquid-gas phase transitions. 1993, *Journal de Physique II*, **3**, 309–337.
- Bagnoli, F., Reichtmann, R., and Zanette, D. Thermodynamics of lattice gas models with discrete velocities. 1993, *Revista Mexicana de Fisica*, **39**, 763–774.
- Beguelin, A.L., Dongarra, J.J., Geist, G.A., Manchek, R.J., and V.S., Sunderam. “A users’ guide to PVM parallel virtual machine”. Technical Report ORNL/TM-11826, Oak Ridge National Laboratory, Oak Ridge TN, July 1991.
- Behrend, O., Harris, R., and Warren, P.B. Hydrodynamic behavior of Lattice Boltzmann and Lattice BGK models. 1993, *electronic preprint: comp-gas/9308001*, .
- Bernoulli, Daniel. *Hydrodynamica, sive de viribus et motibus fluidorum commentarii*. Argentorati, 1738.
- Bhatnagar, P.L., Gross, E.P., and Krook, M. 1954, *Phys. Rev.*, **94**, 511.
- Blitz, Leo. Giant molecular clouds. In Levy, Eugene H. and Lunine, Jonathan I., editors, *Protostar and Planets III*, pages 125–162, Tucson & London, 1993. The University of Arizona Press.
- Boghosian, B.M. Lattice gas hydrodynamics. 1993, *Nuclear Physics B, Proceedings Supplements*, **30**, 204–210.
- Boltzmann, L. Studien über das Gleichgewicht der lebendigen Kraft zwischen bewegten materiellen Punkten. 1868, *Wien. Ber.*, **58**, 517.
- Boulanger, F. and Péroult, M. Diffuse infrared emission from the galaxy. I. Solar neighborhood. 1988, *Ap.J.*, **330**, 964–985.
- Brandes, Th. “Compiling Data Parallel Programs to Message Passing Programs for Massively Parallel MIMD Systems”. In “*Working Conference on MASSIVELY PARALLEL PROGRAMMING MODELS: Suitability, Realization, and Performance*”, Berlin, September 1993.
- Chen, H., Doolen, G.D., Lee, Y.C., and Rose, H. 1989, *Phys. Rev. A*, **40**, 2850.

- Chen, S., Martinez, D.O., Matthaeus, W.H., and Chen, H. Magnetohydrodynamics computations with lattice gas automata. 1992, *J. Stat. Phys.*, **68**(3-4), 533–556.
- Chen, Y., Ohashi, H., and Akiyama, M. The Lattice Boltzmann Equation Method for the Simulation of Compressible Fluid Flow. In *Proceedings of the 1993 Simulation MultiConference*, 1993.
- Chen, Y., Ohashi, H., and Akiyama, M. Thermal lattice Bhatnagar-Gross-Krook model without nonlinear deviations in macrodynamic equations. 1994, *Physical Review E*, **50**, 2776–2783.
- Chopard, B., Droz, M., Cornell, S., and Frachebourg, L. Cellular automata approach to reaction-diffusion systems: theory and application. In *Workshop on Cellular Automata for Astrophysical Phenomena*, 1993. World Scientific.
- Conway, John Horton. *Life*, 1968. University of Cambridge.
- Cox, P. Private communication. 1995.
- D’Humières, D., Lallemand, P., and Frisch, U. Lattice Gas Models for 3D Hydrodynamics. 1986, *Europhys. Lett.*, **2**(4), 291.
- Dubrulle, B., Frisch, U., Hénon, M., and Rivet, J.-P. Low-Viscosity Lattice Gases. 1990, *J. Stat. Phys.*, **59**(5/6), 1187–1226.
- Elias, J.H. 1978, *Ap.J.*, **224**, 857.
- Falgarone, E. and Phillips, T.G. 1990, *Ap.J.*, **359**, 344.
- Falgarone, E., Phillips, T.G., and Walker, C.K. 1991, *Ap.J.*, **378**, 186.
- Falgarone, E., Lis, D.C., Phillips, T.G., Pouquet, A., Porter, D.H., and Woodward, P.R. Synthesized spectra of turbulent clouds. 1994, *Ap.J.*, **436**, 728–740.
- Frisch, U., Hasslacher, B., and Pomeau, Y. Lattice Gas Automata for the Navier-Stokes Equation. 1986, *Phys. Rev. Lett.*, **56**(14), 1505.
- Haken, H. *Synergetics. An Introduction*, volume 1 of *Springer Series in Synergetics*. Springer, Berlin, 3rd edition, 1983.
- Hardy, J. and Pomeau, Y. 1972, *J. Math. Phys. (N. Y.)*, **13**, 1042.
- Hardy, J., De Pazzis, O., and Pomeau, Y. 1973, *J. Math. Phys. (N. Y.)*, **14**, 1746.
- Hardy, J., De Pazzis, O., and Pomeau, Y. 1976, *Phys. Rev. A*, **13**, 1949.
- Hénon, M. Isometric Collision Rules for the FCHC Lattice Gas. 1987, *Complex Systems*, **1**, 475.
- Hetem, A., Jr. and Lépine, J.R.D. Fractal 3-D simulations of molecular clouds. 1993, *A.&A.*, **270**, 451–461.
- Higuera, F.J. and Jiménez, J. 1989, *Europhys. Lett.*, **9**(7), 663.
- Higuera, F.J. and Succi, S. 1989, *Europhys. Lett.*, **8**, 517.
- Houlahan, P. and Scalo, J. 1992, *Ap.J.*, **393**, 172.

- Koelbel, C., Loveman, D., Schreiber, R., Steele, G., and Zosel, M. *The High Performance Fortran Handbook*. The MIT Press, Cambridge, MA, 1994.
- Landau, L.D. and Lifschitz, E.M. *Hydrodynamik*. Akademie-Verlag, Berlin, 1966.
- Lang, Kenneth R. *Astrophysical Formulae*. Springer Verlag, Berlin, 1980.
- Langer, W.D., Wilson, R.W., and Anderson, C.H. Hierarchical structure analysis of interstellar clouds using nonorthogonal wavelets. 1993, *Ap.J.*, **408**, L45.
- Langton, C.G. Computation at the edge of chaos: Phase transitions and emergent computation. 1990, *Physica D*, **42**, 12–37.
- Lawniczak, A. and collaborators. 1991, *Physica D*, **47**, 132.
- Lovejoy, S. 1982, *Science*, **216**, 185.
- Lynds, B. Catalogue of dark nebulae. 1962, *Ap.J. Suppl.*, **7**, 1–52.
- Maddalena, R.J. and Thaddeus, P. 1985, *Ap.J.*, **294**, 231.
- Mathis, John S., Rumpl, William, and Nordsieck, Kenneth H. The size distribution of interstellar grains. 1977, *Ap.J.*, **217**, 425.
- Maxwell, J.C. 1860, *Phil. Mag. [4]*, **19**, 19.
- McNamara, G.R. and Alder, B. Analysis of the lattice Boltzmann treatment of hydrodynamics. 1993, *Physica A*, **194**, 218.
- McNamara, G.R. and Zanetti, G. 1988, *Phys. Rev. Letters*, **61**(20), 2332.
- Montgomery, D. and Doolen, G.D. Magnetohydrodynamic cellular automata. 1987, *Phys. Lett. A*, **120**(5), 229–231.
- Moyer, S.A. and Sunderam, V.S. PIOUS for PVM Version 1.2 User's Guide and Reference Manual. Technical report, Department of Mathematics and Computer Science, Emory University, Atlanta, GA 30322, U.S.A., January 1995.
- Myers, P.C. and Benson, P.J. Dense cores in dark clouds II. NH₃ observations and star formation. 1983, *Ap.J.*, **266**, 309–320.
- Myers, P.C. and Khersonsky, K. On Magnetic Turbulence In Interstellar Clouds. 1995, *Ap.J.*, **442**, 186.
- Nickel, G.H. Cellular automaton rules for solving the Milne problem. 1988, *Phys. Lett. A*, **133**(4,5), 219–224.
- Packard, N.H. Adaptation toward the edge of chaos. In Kelso, J.A.S., Mandell, A.J., and Shlesinger, M.F., editors, *Dynamic Patterns in Complex Systems*, pages 293–301, Singapore, 1988. World Scientific.
- Pineau de Forêts, G., Roueff, E., Schilke, P., and Flower, D.R. Sulphur-bearing molecules as tracers of shocks in interstellar clouds. 1993, *Mon. Not. R. Astron. Soc.*, **262**, 915–928.
- Qian, Y.H. *Gaz sur Réseaux et Théorie Cinétique sur Réseaux Appliquée à l'Equation de Navier-Stokes*. PhD thesis, University of Paris, 1990.

- Qian, Y.H. Simulating Thermohydrodynamics with Lattice BGK Models. 1993, *J. Sc. Comp.*, **8**(3), 231–242.
- Qian, Y.H., D’Humières, D., and Lallemand, P. Lattice BGK Models for Navier-Stokes Equation. 1992, *Europhys. Lett.*, **17**(6), 479–484.
- Reynolds, O. 1883, *Phil. Trans. Roy. Soc. London*, **174**, 935.
- Rothman, D.H. and Keller, J.M. 1988, *J. Stat. Phys.*, **52**, 1119.
- Schmid-Burgk, J. and Muders, D. “Beyond HH 7-11: Another Look at the Interstellar Environment of Molecular Outflows”. In Wallerstein, George and Noriega-Crespo, Alberto, editors, *Stellar and Circumstellar Astrophysics*, volume 57 of *ASP Conf. Series*, 1994.
- Somers, J.A. and Rem, R.C. The construction of efficient collision tables for fluid flow computations with cellular automata. In Manneville, P., Boccara, N., Vichniac, G.Y., and R., Bidaux, editors, *Cellular Automata and Modeling of Complex Physical Systems, Proceedings of the Winter School, Les Houches, France*, pages 161–177, February 1989. Springer-Verlag.
- Sterling, James D. and Chen, Shiyi. Stability Analysis of Lattice Boltzmann Methods. 1996, *J. Comp. Physics*, **123**, 196–206.
- Stutzki, J. and Güsten, R. High Spatial Resolution Isotopic CO and CS Observations of M17 SW: The Clumpy Structure of the Molecular Cloud Core. 1990, *Ap.J.*, **356**, 513–533.
- Succi, S., d’Humières, D., Qian, Y.H., and Orszag, S.A. On the Small-Scale Dynamical Behavior of Lattice BGK and Lattice Boltzmann Schemes. 1993, *J. Sc. Comp.*, **8**(3), 219–230.
- TMC. *Connection Machine CM-5 Technical Summary*. Thinking Machines Corporation, 245 First Street, Cambridge, Massachusetts 02142–1264, November 1993.
- Ungerechts, H. and Thaddeus, P. 1987, *Ap.J. Suppl.*, **63**, 645.
- Williams, J.P. and Blitz, L. 1993, *Ap.J.*, **405**, L75.
- Williams, Jonathan P., de Geus, Eugène, and Blitz, Leo. Determining structure in molecular clouds. 1994, *Ap.J.*, **428**, 693–712.
- Wolfram, S. Cellular Automaton Fluids 1: Basic Theory. 1986, *J. Stat. Phys.*, **45**(3/4), 471–526.

Danksagung

Herrn Prof. Schmid-Burgk möchte ich dafür danken, daß er mir bei der Wahl der Thematik sowie der Durchführung dieser Dissertation große Freiheit ließ, mir aber in kritischen Diskussionen immer wieder neue Anregungen und Einsichten vermittelte. Herrn Prof. Fahr danke ich für die freundliche Übernahme des Koreferats. Die Arbeit ist im Rahmen eines Dissertationsstipendiums der Max-Planck-Gesellschaft entstanden.

Für die Simulationen im Max-Planck-Institut für Radioastronomie konnte ich die drei derzeit leistungsfähigsten Rechner vom Typ HP 735⁺ benutzen. Dies wurde durch die Kooperation der Arbeitsgruppen „Molekülspektroskopie“, „Pulsare“ und „VLBI“ ermöglicht. Für die Koordination danke ich Herrn Prof. Fürst und Herrn Dr. Peter Müller. Unzählige Hard- und Softwareprobleme wurden bis zur letzten Minute von Dr. Peter Müller, Ingo Kruhm, Dipl.-Phys. H.-G. Girnstein, Dr. J. Schmidt, Dipl.-Phys. A. v. Kap-herr und J. Elter gelöst. Herr Dr. Engelen wußte immer Rat bei Fragen zu \LaTeX und Farbausdrucken. Dipl.-Phys. Gereon Dahmen entwickelte mit „astro-cite.sty“ die astronomische Ergänzung zu \LaTeX . Den Operateuren in Effelsberg danke ich für die Unterstützung bei den 30 GHz Messungen. Dr. Keven Uchida und Dipl.-Phys. Achim Tieftrunk übernahmen den Großteil des Korrekturlesens. Herr Dr. Peter Ossadnik (GMD, TMC) half mir intensiv bei der Umsetzung und Optimierung des Hydrodynamikprogramms für den Parallelrechner „CM-5“ der GMD in St. Augustin. Die Farbausdrucke für diese Arbeit wurden bei Minolta Plankopie in Köln angefertigt.

Allen Freunden und Bekannten danke ich dafür, daß sie zur richtigen Zeit am richtigen Ort waren. Meinen Eltern bin ich zu besonderem Dank verpflichtet, da sie den langen Weg bis zu dieser Arbeit begleitet und gefördert haben. Annette Landsberg danke ich für ihre Zuneigung, ihr Verständnis und die schöne Zeit in der normalen Welt.

Lebenslauf

Dirk Muders, geboren am 10. März 1966 in Boppard am Rhein als erstes Kind von Ingrid Muders geb. Lief und Karl Muders

- 1972–1976: Besuch der Grundschule in St. Goar
- 1976–1985: Stefan-George-Gymnasium in Bingen / Rhein
- Juni 1985: Abitur
- WS 1985/86: Beginn des Physikstudiums an der Johannes-Gutenberg-Universität Mainz
- Oktober 1987: Vordiplom in Physik
- SS 1988: Wechsel zur Rheinischen Friedrich-Wilhelms-Universität Bonn zur Fortsetzung des Studiums der Physik und zur Aufnahme des Studiums der Astronomie
- Sommer 1989: Teilnahme an der Sommerschule des Max-Planck-Instituts für Plasmaphysik in Garching bei München
- Mai 1990: Mündliche Diplomprüfung in Physik: Theoretische Physik, Experimentalphysik (Schwerpunkt Elementarteilchenphysik), Angewandte Physik (Radioastronomische Meßtechnik), Nebenfach Astronomie
- November 1990: Beginn der Diplomarbeit am Max-Planck-Institut für Radioastronomie Bonn; Betreuer: Prof. Dr. Schmid-Burgk
- WS 1991/92: Beginn des Zweitstudiengangs Magister Indologie mit den Nebenfächern Theoretische Physik und Sprachwissenschaft an der Universität Bonn
- Juli 1992: Abschluß des Physikstudiums mit der Diplomarbeit über „Linienemission rotierender Gaswolken: Beobachtungen und Modelle“
- Seit August 1992: Dissertationsstipendium der Max-Planck-Gesellschaft; Vorbereitung der vorliegenden Dissertation am Max-Planck-Institut für Radioastronomie; Sanskrit und Hindi als Promotionsnebenfach